

This is the Accepted Manuscript version of the paper.

The full published version of Lambert-Smith, James S., Allibone, Andrew, Treloar, Peter J., Lawrence, David M., Boyce, Adrian J. and Fanning, Mark (2020) Stable C, O, and S isotope record of magmatic-hydrothermal interactions between the Falémé Fe Skarn and the Loulo Au Systems in Western Mali. *Economic Geology*, 115(7), pp. 1537-1558. can be found at <https://doi.org/10.5382/econgeo.4759>

1 **Stable C, O and S Isotope Record of Magmatic-Hydrothermal Interactions**  
2 **Between the Falémé Fe Skarn and the Loulo Au Systems in Western Mali**

3 **James S. Lambert-Smith<sup>1\*</sup>, Andrew Allibone<sup>2</sup>, Peter J. Treloar<sup>3</sup>, David M. Lawrence<sup>2</sup>,**  
4 **Adrian J. Boyce<sup>4</sup>, Mark Fanning<sup>5</sup>**

5 <sup>1</sup>School of Earth and Ocean Sciences, Cardiff University, Main Building, Park Place, Cardiff, CF10 3AT,  
6 UK

7 <sup>2</sup>Barrick Gold (Holdings) Ltd, 3rd Floor, Unity Chambers, 28 Halkett St., St Helier, Jersey JE2 4WJ,  
8 Channel Islands, UK

9 <sup>3</sup>School of Natural and Built Environments, Kingston University London, Kingston upon Thames, KT1  
10 2EE

11 <sup>4</sup>Scottish Universities Environmental Research Centre, East Kilbride, Glasgow, Scotland, G75 0QF

12 <sup>5</sup>Research School of Earth Sciences, Australian National University, Canberra ACT0200, Australia

13 \*Corresponding author email address: [lambert-smithj@cardiff.ac.uk](mailto:lambert-smithj@cardiff.ac.uk)

14 **Keywords:** Stable isotopes; Loulo Mining District; Birimian; Orogenic gold mineralization; Iron skarns

15 **Abstract**

16 The Gara, Yalea and Goukoto Au deposits of the 17+ Moz Loulo Mining District, largely hosted by  
17 the Kofi Series metasediments, are located several kms to the east of the 650 Mt Fe skarn deposits in  
18 the adjacent Falémé Batholith. The Au deposits are interpreted to have formed through phase separation  
19 of an aqueous-carbonic fluid, which locally mixed with a hypersaline brine of meta-evaporite origin.  
20 Recognition of an intrusive relationship between the Falémé Batholith and Kofi Series opens the  
21 possibility that the Fe skarns and Au deposits are part of the same mineral system. In this paper, we  
22 combine new  $\delta^{13}\text{C}$ ,  $\delta^{18}\text{O}$  and  $\delta^{34}\text{S}$  data from the Karakaene Ndi skarn, minor Au occurrences along the  
23 western margin of the Kofi Series, and zircons within plutonic rocks of the Falémé Batholith with  
24 existing data from the Loulo Au deposits, to model the contribution of magmatic volatiles to Au  
25 mineralization.

26 C- and O-isotope compositions of auriferous carbonate-quartz-sulfide veins from the Loulo Au deposits  
27 have wide ranges ( $\delta^{13}\text{C}$ :  $-21.7$  to  $-4.5$  ‰ and  $\delta^{18}\text{O}$ :  $11.8$  to  $23.2$  ‰), whereas values from carbonate  
28 veins in Kofi Series Au prospects close to the Falémé Batholith, and the Karakaene Ndi Fe skarn  
29 deposit, have more restricted ranges ( $\delta^{13}\text{C}$ :  $-16.8$  to  $-3.7$  ‰,  $\delta^{18}\text{O}$ :  $11.4$  to  $17.2$  ‰ and  $\delta^{13}\text{C}$   $-3.0 \pm 1$  ‰,  
30  $\delta^{18}\text{O}$   $12.6 \pm 1$  ‰, respectively). Kofi Series dolostones have generally higher isotopic values ( $\delta^{13}\text{C}$ :  $-$   
31  $3.1$  to  $1.3$  ‰ and  $\delta^{18}\text{O}$ :  $19.1$  to  $23.3$  ‰). Pyrite from Kofi Series Au prospects adjacent to the Falémé

32 Batholith, have a wide range of  $\delta^{34}\text{S}$  values (−4.6 to 14.2 ‰), similar to pyrite from the Karakaene Ndi  
33 skarn (2.8 to 11.9 ‰), whereas  $\delta^{34}\text{S}$  values of pyrite and arsenopyrite from the Loulo deposits are  
34 consistently > 6 ‰.

35 Comparison of the C- and O-isotopic data with water-rock reaction models indicates the Loulo Au  
36 deposits formed primarily through unmixing of an aqueous carbonic fluid derived from the  
37 devolatilisation of sedimentary rocks with an organic carbon component. Isotopic data are permissive  
38 of the hypersaline brine which enhanced this phase separation including components derived from both  
39 Kofi Series evaporite horizons interlayered with the dolostones and a magmatic-hydrothermal brine.  
40 This magmatic-hydrothermal component is particularly apparent in O-, C-, and S-isotopic data from the  
41 Gara deposit and Au prospects immediately adjacent to the Falémé Batholith.

43 Orogenic deposits account for ~30 % of total Au production, reserves, and resources (Frimmel and  
44 Hennigh, 2015), making them one of the most important sources of Au globally. Most of these deposits  
45 formed from near neutral low salinity aqueous-carbonic fluids at temperatures between 250-400°C in  
46 greenschist facies metamorphic terranes (e.g. Groves et al., 1998; Goldfarb et al., 2005; Phillips and  
47 Powell, 2010; Goldfarb and Groves, 2015). There is widespread consensus that metasedimentary and /  
48 or metabasaltic rocks undergoing metamorphic devolatilization reactions are the ultimate source of the  
49 ore fluids in orogenic gold deposits, with the metals scavenged from the same rocks (Henley et al.,  
50 1976; Norris and Henley, 1976; Kerrich and Wyman, 1990; Goldfarb et al., 1991; Phillips and Powell,  
51 1993; McCuaig and Kerrich, 1998; Pitcairn et al., 2006, Gaboury, 2013; Tomkins, 2013; Pitcairn et al.,  
52 2014; Yardley and Cleverley, 2015; Goldfarb and Groves, 2015; Wyman et al., 2016; Groves et al.,  
53 2019). However, speculation remains that some deposits include hydrothermal fluids exsolved from  
54 crystallizing magmas (Lawrence et al., 2013a, 2013b; Xue et al., 2013; Treloar et al., 2015; Spence-  
55 Jones et al., 2018). Resolving this question is an important part of the development of a holistic mineral  
56 system model for orogenic Au deposits (Wyman et al., 2016; Groves et al., 2019).

57 The 17+ Moz Loulo Au Mining District in the Kédougou-Kéniéba inlier in western Mali and eastern  
58 Senegal is one of the most richly endowed orogenic Au districts in the West Africa craton (Fig. 1). It  
59 includes three major multi-million ounce deposits, including Gara, Yalea, and Goukoto and numerous  
60 satellite deposits that typically contain <1 Moz Au (e.g., Baboto, Faraba, Loulo 3, Loulo 2, P64, and  
61 P129). Small-displacement, discontinuous shear-zones, some of which may have nucleated along earlier  
62 fold axial planes. Quartz-tourmaline-altered quartz gritstone units within the Kofi Series siliciclastic,  
63 carbonate, and evaporitic rocks host the Au deposits. The western margin of the Kofi Series is intruded  
64 and unconformably overlain by high-K plutonic rocks of the Falémé Batholith and related Bambadji  
65 Formation volcanic rocks, respectively. Magnetite and hematite-rich endoskarns, which contain > 650  
66 Mt Fe, are present within the Falémé Batholith. Related exoskarns locally extend into the Bambadji  
67 Formation and the western-most parts of the Kofi Series, further demonstrating the intrusive  
68 relationship between the Falémé Batholith and Kofi Series at the time skarn mineralization occurred.

69 Despite several detailed studies of the Au deposits (Fouillac et al., 1993; Lawrence et al., 2013a;  
70 Lawrence et al., 2013b; Lambert-Smith et al., 2016b; Lambert-Smith et al., 2016c), the ultimate source  
71 of fluids and Au in the Loulo mineral system remains uncertain. Lawrence et al. (2013b) proposed a  
72 magmatic contribution to auriferous fluids due to the presence of a high-temperature (>400 °C)  
73 hypersaline brine in several deposits. However, Lambert-Smith et al. (2016b) argued against a  
74 magmatic source for the brines on the basis of B, S, C, and O isotopic data. In particular, B-isotope data  
75 indicate derivation of brines from evaporite units in the Kofi Series (Lambert-Smith et al., 2016c).  
76 Nevertheless, the Falémé Batholith and associated skarns intrude and extend into the Kofi Series,



77 instead of being separated by a terrane boundary (Senegal-Mali Shear Zone), reopens the possibility  
78 that the Falémé Fe magmatic-hydrothermal system contributed to Au mineralization at Loulo.  
79 Furthermore, Masurel et al. (2017c) report direct overprinting of calc-silicate skarn mineralization by  
80 biotite-calcite-quartz  $\pm$  K-feldspar-tourmaline-actinolite alteration associated with Au mineralisation at  
81 the Sadiola Hill Au deposit. The deposit is carbonate-hosted and located in the northern part of the  
82 Kédougou-Kéniéba inlier in the vicinity of an intrusive centre correlative with the Falémé Batholith.

83 The Baqata, Kolya, Kabe West and Gefa (Fig. 2) prospects are hosted in the Kofi Series, less than 2 km  
84 from the intrusive contact with the Falémé Batholith. Minor Au-bearing veins are also present within  
85 the Falémé Batholith, at the Boboti target. These Au occurrences, within the batholith and midway  
86 between the batholith margin and major Au deposits of the Loulo Mining District, provide an  
87 opportunity to examine the genetic links between the Falémé Fe skarns (Schwartz and Melcher, 2004)  
88 and the Loulo Au deposits. Furthermore, samples from the Karakaene Ndi Fe skarn deposits provide  
89 data on the isotopic character of the Fe skarns and any local magmatic-hydrothermal contribution to the  
90 Au deposits. Here we use new C, O and S isotope data from these Au occurrences and from the  
91 Karakaene Ndi skarn, together with existing isotopic data from Gara, Yalea and Goukoto (Fouillac et  
92 al., 1993; Lawrence et al., 2013b; Lambert-Smith et al., 2016b), as tracers for the source to ore pathways  
93 of auriferous fluids. The magmatic contribution, if any, to Au mineralization in the Kofi Series is based  
94 on new Sensitive High-Resolution Ion Microprobe (SHRIMP)  $\delta^{18}\text{O}$  analyses of magmatic zircons  
95 recovered from the Falémé Batholith.

96

### Geological Setting

97 The 2.27 to 2.05 Ga Paleoproterozoic terranes of the southern West African Craton constitute one of  
98 the world's leading Au-provinces, with an overall endowment in excess of 350 Moz (Goldfarb et al.,  
99 2017; Thebaud et al., in press). Paleoproterozoic rocks are exposed in the Baoulé-Mossi domain, the  
100 Kédougou-Kéniéba and Kayes inliers (Fig. 1), and in the eastern Reguibat Rise in North Africa. They  
101 include shear-bounded, linear and arcuate belts of volcano-sedimentary rocks ca. 2270-2150 Ma old  
102 (e.g. Baratoux et al., 2011), younger sedimentary basins ca. 2135-2095 Ma old (e.g. Taylor et al., 1992;  
103 Lebrun et al., 2015), and granitoid-dominated terranes ca. 2190-2060 Ma old (e.g. Hirdes et al., 1992;  
104 Parra-Avila et al., 2017) . The volcano-sedimentary belts largely comprise lavas of tholeiitic and calc-  
105 alkaline affinity, volcanoclastic rocks, and epiclastic sedimentary rocks. The basins are filled with  
106 siliciclastic rocks, including arkoses, greywackes, argillites, arenites, and rare limestones and chemical  
107 sediments. Multiple suites of granitoid rocks intrude both the belts and the basins.

108 The Paleoproterozoic terranes formed, accreted, and were deformed over  $\sim$ 200 Myr (e.g. Perrouty et  
109 al., 2012; White et al., 2014; Parra-Avila et al., 2016; Grenholm et al., 2019; Thebaud in press) during  
110 the 2266-2140 Ma Eoeburnean , and 2135-2050 Ma Eburnean periods (e.g. Taylor et al., 1992; Dia et  
111 al., 1997; Loh et al., 2000; Allibone et al., 2002; Gueye et al., 2007; Hein, 2010; De Kock et al., 2011;

112 Baratoux et al., 2011; Tshibubudze et al., 2015). Initial volcanism, granitoid emplacement, fold and  
113 thrust tectonics, and metamorphism took place during Eoeburnean crustal growth and accretion. The  
114 ages of the youngest detrital zircon populations indicate that the sedimentary basins developed from  
115 2135 to 2095 Ma (Davis et al., 1994; Oberthür et al., 1998; Hirdes and Davis, 2002; Vidal et al., 2009;  
116 Lebrun et al., 2016). Emplacement of younger granitoid plutons (Parra-Avila et al., 2018; Masurel et  
117 al., 2017a), further contractional deformation and metamorphism, late strike-slip deformation, and  
118 widespread Au mineralization occurred during the subsequent Eburnean orogeny (Oberthür et al., 1998;  
119 McFarlane et al., 2011; Parra-Avila et al., 2015; Fontaine et al., 2017; Fougrouse et al., 2017; Masurel  
120 et al., 2017b). Greenschist facies mineral assemblages dominate in most Paleoproterozoic rocks across  
121 West Africa, but amphibolite and granulite facies assemblages are present locally within both the  
122 Eoeburnean belts and Eburnean sedimentary basins (John et al., 1999; White et al., 2014; MacFarlane  
123 et al., 2019). Particularly low geothermal gradients of 10-12° C km<sup>-1</sup> are consistent with modern  
124 subduction processes during Eburnean time in some parts of the craton (Ganne et al., 2011; Block et al.  
125 2015).

126

### **Geology of the Loulo Mining District**

127 The Kofi Series comprises metamorphosed immature detrital sedimentary and carbonate rocks  
128 deposited after 2120-2100 Ma. The former are dominantly sandstones, wackes, and argillites that  
129 include both quartz- and feldspar-rich siliciclastic components. Carbonate lithologies are more abundant  
130 in the west, close to the contact with the Falémé Batholith (Fig. 2). These are dominantly dolomitic,  
131 with mm to cm-scale marl horizons that contain clasts of fine-grained, sub-angular quartz and feldspar  
132 and very fine-grained muscovite. Carbonate lithologies also contain a minor graphitic-argillaceous  
133 component, present as mm to sub-mm scale lamellae, or as fine rounded and strained clasts. The Kofi  
134 Series sedimentary rocks were tilted upright, tightly folded, cut by reverse faults, and metamorphosed  
135 under upper greenschist facies biotite zone conditions during D<sub>1</sub> contractional deformation between ca.  
136 2100-2090 Ma. Later small-scale (< 1 km) folding and development of an associated steeply dipping  
137 axial planar cleavage, and Au mineralization occurred during D<sub>2</sub> sinistral transcurrent deformation  
138 between ca. 2085 and 2060 Ma (Hirdes and Davis, 2002; Schwartz and Melcher, 2004; Lawrence et al.,  
139 2013a; Masurel et al., 2017a; Masurel et al., 2017b). The Falémé Batholith, and associated outlying  
140 plutons and dikes, intruded the Kofi Series between 2084 ± 8 Ma and 2075 ± 6 Ma, after inversion of  
141 the Kofi Series during D<sub>1</sub> contraction. Outlying dikes of the Falémé batholith at Goukoto and Gara  
142 have been affected by the later stages of hydrothermal activity and syn-Au deformation indicating  
143 magmatism occurred during the earlier stage(s) of D<sub>2</sub>, prior to mineralisation, but nevertheless part of  
144 the same overall D<sub>2</sub> event. While the exact timing of mineralization is yet to be determined, these  
145 relationships suggest magmatic activity and Au mineralization were broadly synchronous.

146 Lawrence et al. (2013a, b) describe two end-member styles of Au mineralization at Loulo, termed Gara-  
147 and Yalea-style, respectively. Gara-style deposits are characterized by pyrite dominated ores with metal  
148 signatures enriched in Fe-Rare Earth Element (REE)-W and rare base metals. Intense tourmaline  
149 alteration, which is atypical of orogenic Au deposits (e.g. Groves et al., 1998), and hypersaline fluid  
150 inclusions further characterise this style of mineralization (Lawrence et al., 2013b). Conversely, Yalea-  
151 style deposits are As-rich and lack REE and base metal enrichment. Alteration assemblages consist of  
152 early quartz-carbonate-albite, overprinted by sericite-chlorite-sulfide-Au (Lawrence et al., 2013a).  
153 Fluids are dilute and aqueous-carbonic in character (Lawrence et al., 2013b). The Goukoto deposit  
154 exhibits characteristics in common with both styles, including hypersaline fluid inclusions and As-rich  
155 sulfide assemblages (Lambert-Smith et al., 2016b). Satellite deposits and exploration targets in the  
156 region display characteristics of either style (Lawrence et al., 2013a; Lambert-Smith, 2014a). All Au  
157 and Fe mineralization in the district is associated with moderate to intense albitization, which affects  
158 most rock types.

159 Lawrence et al. (2013b) interpreted fluid inclusion assemblages as representing two distinct end-  
160 member fluids: 1) a high T, high-salinity, CO<sub>2</sub>-poor, aqueous fluid (~400°C; ~45-55 wt. % NaCl equiv.);  
161 and 2) a moderate T, dilute, aqueous-carbonic fluid (270-350°C; <10 wt. % NaCl equiv.). Partial mixing  
162 between these fluids at Gara-style ore bodies resulted in retrograde boiling and changes in the  
163 physicochemical state of both fluids leading to sulfide mineralization and Au precipitation (Lawrence  
164 et al., 2013a, b). At Yalea, the hypersaline fluid is absent and fluid inclusion assemblages feature two  
165 immiscible phases derived from phase separation of a dilute aqueous-carbonic fluid (Lawrence et al.,  
166 2013b). This likely occurred in response to a combination of fluid-rock interaction, particularly  
167 sulfidation, and pressure fluctuations along the brittle-ductile host structures. Stable isotope data from  
168 Au-related quartz ( $\delta^{18}\text{O}$  from 12.9 to 17.4 ‰), dolomite ( $\delta^{13}\text{C}$  from -21.7 to -4.5 ‰), and pyrite ( $\delta^{34}\text{S}$   
169 from 5.8 to 15.5 ‰) (Lawrence et al., 2013b) at Gara, Yalea and Goukoto are generally consistent  
170 with fluids being sourced from the devolatilization of Kofi Series metasedimentary rocks (Lambert-  
171 Smith et al., 2016b), though  $\delta^{18}\text{O}$  and  $\delta^{13}\text{C}$  values partially overlap magmatic fields. Furthermore, B-  
172 isotope data from hydrothermal tourmaline indicates a meta-evaporite source for B, implying evaporite  
173 devolatilization in the genesis of the hypersaline brine (Lambert-Smith et al., 2016c).

#### 174 *Au and Fe mineralization in the western Kofi series and Falémé Batholith*

175 The minor Au occurrences along the western margin of the Kofi Series at Baqata, Kolya, Kabe West,  
176 Boboti and Gefa (Fig. 2) have been described in detail by (Lambert-Smith, 2014a). The key geological  
177 characteristics of these occurrences and the larger deposits are summarized in Table 1.

178 Baqata is located ~6.2 km SE of Goukoto (Fig. 2). Mineralization is hosted in a package of altered  
179 Kofi Series quartz wacke, dolostone, and argillite interbedded with siltstones and sandstones, which  
180 dips 60° W and strikes 185°. Bedding is cut by a sub-vertical NNE-striking cleavage which is axial

181 planar to 100 m-scale SSW plunging asymmetric  $F_2$  folds. The sequence is intruded by 1-10 m thick,  
182 variably albitized diorite and monzodiorite dikes, and cut by steeply dipping NNW-striking (80E/350)  
183 shear zones. Mineralized rocks include both Gara-style ankerite-quartz-pyrite stockworks in  
184 tourmalinized quartz wacke and disseminated pyrite and chlorite-pyrite stringers in albitized dolostone  
185 and quartz wacke. Au grades locally reach 13.4 g/t but are discontinuous along strike and down-dip.  
186 Like at Gara, accessory Ni-sulfides (e.g. millerite), xenotime, and monazite are present. Gold,  
187 tellurobismuthite ( $\text{Bi}_2\text{Te}_3$ ), calaverite and bismuth are occluded in pyrite and the gangue.

188 At Kolya, ~13 km south of Gara, discontinuous zones of mineralized rock that contain up to ~5.8 g/t  
189 Au are hosted in a package of argillites, greywackes, tourmalinized quartz wackes, and dolostones,  
190 which dips  $70^\circ$  W and strikes  $350^\circ$ . These rocks are folded, cleaved, and cut by shear zones in the same  
191 manner as those at Baqata. Dolerite dikes intrude the sedimentary rock package. Mineralized rocks at  
192 Kolya comprise chlorite-pyrite veins primarily within the dolerite dikes, and minor hydrothermal  
193 breccias and ankerite-quartz-pyrite vein stockworks in tourmalinized quartz wacke. Gold occurs as  
194 occluded grains and fracture-fill in pyrite and arsenian pyrite, where it is associated with minor altaite  
195 ( $\text{PbTe}$ ), melonite ( $\text{NiTe}_2$ ) and tellurobismuthite. Kolya lacks Ni-sulfide phases.

196 Kabe West is located ~2.5 km south west of Kolya. Gold is hosted in intensely albitized igneous rocks  
197 which intrude albitized dolostone, siliciclastic rocks and hydrothermal breccias. Gold grades are  
198 typically 2-4 g/t (locally up to 11.3 g/t) and spatially discontinuous. Structural controls on  
199 mineralization are not known due to poor exposure, lack of oriented drill core, and overprinting of pre-  
200 mineralization fabrics by intense albitization. Pyrite is the dominant ore phase and contains up to 1.9  
201 wt. % Co and 0.5 wt. % Ni. Gold, altaite and melonite occur as inclusions within, or annealed to, pyrite  
202 grains, which are disseminated in albitized wall rock and in hydrothermal breccias with tourmaline or  
203 dolomite cement.

204 Mineralized rocks at Gefa, ~7 km south of Baqata, are hosted in a package of albitized argillite,  
205 dolostone, and greywacke. The host sedimentary rocks strike N-S and dip  $80^\circ$  W and are intruded by  
206 unmineralized diorite and quartz feldspar porphyry dikes. These rocks are cut by sheared polymict  
207 hydrothermal breccias. Mineralized rocks are generally characterized by Au grades  $< 0.5$  g/t, localized  
208 within zones of brittle quartz-carbonate-pyrite veining that cross cut intensely albitized rock.

209 Boboti is located ~8.3 km to the south west of Baqata. Mineralization is hosted in albitized subvolcanic  
210 andesites and medium to coarse-grained diorites of the Boboti Pluton. Gold is hosted by pyrite grains  
211 within carbonate-pyrite veinlets and minor disseminated pyrite in the immediate wall rock to veins.  
212 Grades reach a maximum of 2.6 g/t Au, but mineralized zones are rarely continuous over more than 1  
213 meter downhole.

214 The Falémé Iron District (Schwartz and Melcher 2004) endo- and exoskarn deposits are located within  
215 the Falémé Batholith, associated altered Bambadji Formation volcanic rocks, and western-most parts  
216 of the Kofi Series (Fig. 2). In the skarns, proximal halos of calc-silicate alteration (actinolite-epidote-  
217 allanite-titanite  $\pm$  clinopyroxene-garnet) overprint regional albitization (Fig.3 a-e). This is further  
218 overprinted by massive magnetite  $\pm$  apatite ore (Fig. 3f). Late sulfide mineralization which typically  
219 includes coarse disseminated pyrite and chalcopyrite, or pyrite-chalcopyrite-calcite veins cuts the iron  
220 ore (Fig. 3f, g). These sulfides are locally auriferous, typically containing  $< 0.5$  g/t Au and rarely up to  
221 3 g/t Au associated with trace amounts of Co-Ni-U-bearing phases. Preliminary fluid inclusion studies  
222 by Schwartz and Melcher (2004) and Lambert-Smith (2014a) tentatively indicate a H<sub>2</sub>O-NaCl-CO<sub>2</sub>  
223 magmatic fluid, with low salinity (approx. 3.3 wt. % NaCl equiv.) and XCO<sub>2</sub> = 0.11. The alteration and  
224 ore mineralogy of the skarns share commonalities with Fe-oxide apatite deposits, and their close spatial  
225 association with a large orogenic Au camp hints at IOCG affinities (Schwartz and Melcher 2004,  
226 Lawrence et al. 2013a).

227

### Sample characteristics and Methods

228  $\delta^{13}\text{C}$  and  $\delta^{18}\text{O}$  was measured in 28 samples from the Kolya, Baqata, Boboti, Gefa and Kabe West  
229 exploration targets and 7 samples from the Karakaene Ndi skarn (Fig. 2). These data include ankerite,  
230 calcite and dolomite from auriferous, skarn-related, and barren hydrothermal veins and wall rock  
231 alteration, and dolomite from host dolostone units (Fig. 4a). A further 49  $\delta^{13}\text{C}$  and  $\delta^{18}\text{O}$  analyses are  
232 included from published data for Goukoto (Lambert-Smith et al., 2016b); Gara (Fouillac et al., 1993 ;  
233 Lawrence et al., 2013b), and Yalea (Lawrence et al., 2013b).  $\delta^{34}\text{S}$  was measured in 23 pyrite samples  
234 from Kolya, Baqata, Boboti and Kabe West exploration targets and in 11 pyrite samples from the  
235 Karakaene Ndi skarn. Zircon  $\delta^{18}\text{O}$  values were measured by SHRIMP on 3 samples of quartz  
236 monzodiorite and quartz monzonite from the Falémé Batholith (RG10036, RG10039, RG10050) and  
237 one sample of Bambadji Formation andesitic volcanoclastic rock (RG10030).

#### 238 *Mineralized vein characteristics*

239 Tourmalinized quartz wacke units are important ore hosts at Gara and the P-64 satellite, subordinate  
240 ore hosts at Goukoto, and host sub-economic mineralization at the Baqata and Kolya targets.  
241 Tourmalinization involves the replacement of the matrices of wackes with cryptocrystalline tourmaline,  
242 making the unit more brittle and therefore susceptible to the development of ankerite-quartz-pyrite-Au  
243  $\pm$  dolomite  $\pm$  tourmaline hydro fracture vein stockworks (Fig. 4b). These stockworks contain several  
244 vein morphologies characteristic of the brittle-ductile environment, including planar centimeter- to  
245 millimeter-scale veins and veinlets, brecciated and boudinaged veins, and sigmoidal vein arrays.  
246 Veining is typically multi-generational, occurring in multiple orientations and at multiple scales ( $< 100$   
247  $\mu\text{m}$  to  $\sim 2\text{-}3$  cm vein width). This stockwork style of mineralization typically affects  $\sim 1$  to 20 m thick

248 units and is associated with Au grades up to ~100 g/t. High grades are generally associated with strongly  
249 altered host rocks, high carbonate and sulfide content in the veins, and the most intense vein networks  
250 with several generations of veins. Veins at Gara commonly include late, gray, quartz-pyrite-Au cores  
251 (Lawrence et al., 2013b).

252 In contrast, veining is a minor part of the mineralized rocks at Yalea and Goukoto, which include a  
253 larger proportion of sulfide stringers, disseminations in the matrix of hydrothermal breccias, and  
254 chloritic ductile shear zones. Mineralized veinlets at Yalea cross-cut ductile shear fabrics, and contain  
255 arsenopyrite-pyrite-arsenian pyrite-Au  $\pm$  quartz  $\pm$  ankerite (Fig. 4c). At Goukoto quartz-carbonate-  
256 pyrite-chlorite veins commonly occur several 10s of meters outside the main ore zone and are associated  
257 with grades up to ~5 g/t Au. Veins are typically undeformed and may cross-cut earlier Au  
258 mineralization. Mineralogically similar veins have been observed in high grade ore shoots but are  
259 typically highly deformed and overprinted by later Au mineralization. Sulfides occupy up to 50 vol. %  
260 of the vein assemblage (more typically ~20 %), and carbonate mineralogy is commonly dolomitic and  
261 rarely ankeritic. Vein width varies from <100  $\mu$ m up to 6-7 cm. Many veins have been reactivated and  
262 brecciated by later hydrothermal events. Undeformed hydrofracture veins and veinlets are also common  
263 at the Baqata, Boboti, Gefa and Kabe West exploration targets.

264 At the Karakaene Ndi skarn, veining generally postdates the oxide ore. Veins are <1 mm to 6 cm thick  
265 and composed of <100  $\mu$ m to >5 mm calcite-pyrite  $\pm$  quartz  $\pm$  chlorite  $\pm$  Au, with pyrite  $\approx$  calcite (Fig.  
266 3g). Sulfide-rich veins do not show the zoned calc-silicate alteration halos characteristic of primary  
267 oxide mineralization.

268 A small number of veins sampled from the Kofi Series were classified as mineralized based on the  
269 presence of sulfide minerals, despite returning fire assay results below detection limit (<0.01 ppm).  
270 These veins contain fine pyrite and chalcopyrite in variable abundance. Several of these veins contain  
271 only one or two sub-mm-scale grains of pyrite or chalcopyrite (Fig. 4d), while others contain several  
272 modal percent of coarse pyrite (some with multiple generations) (Fig. 4g).

### 273 *Barren vein characteristics*

274 Barren hydrothermal veining occurs throughout the Loulo Mining District (Fig. 4e-f). Pre-  
275 mineralization barren quartz-carbonate veins are deformed and display asymmetric fold patterns (Fig.  
276 4f). Late-stage barren quartz-carbonate veins, including at Gara, Yalea, and Goukoto, cross cut  
277 mineralization and alteration (Lawrence et al., 2013a). Elsewhere in the district, similar veining cross  
278 cuts barren country rock (Fig. 4e). These late veins are typically undeformed. The timing of veins  
279 occurring outside the footprint of the large deposits is somewhat uncertain; it is possible that some of  
280 these veins are barren equivalents to mineralized veins. The mineralogy in barren veins comprises

281 variable proportions of quartz-dolomite ± chlorite, with no sulfide minerals present. Vein width ranges  
282 from <1 mm to approximately 8 cm (typically <1 cm).

### 283 *Analytical procedures*

284 *Energy-dispersive X-ray spectroscopy* - Mineral compositions were determined using an Oxford  
285 Instruments X-ACT Energy Dispersive System detector mounted on a Zeiss EVO 50 Scanning Electron  
286 Microscope at Kingston University London. The EDS employed an accelerating voltage of 20 kV, a  
287 beam current of 1.5 nA, and a detector process time of 4 seconds. The detection limit for all elements  
288 was ~0.2 wt. %.

289 *Stable isotopes in carbonates and pyrite*- Carbon and oxygen isotopic analyses of carbonate minerals  
290 were carried out at the Scottish Universities Environmental Research Centre (SUERC) in East Kilbride,  
291 Scotland. CO<sub>2</sub> was liberated via *in vacuo* reaction with 100 % phosphoric acid at 100 °C for dolomite  
292 and ankerite, and at 25 °C for calcite. The CO<sub>2</sub> was analysed on a VG SIRA 10 mass spectrometer. Data  
293 were corrected using oxygen fractionation factors for acid-extracted CO<sub>2</sub> at 100 °C of 1.00913 and  
294 1.00901 for dolomite and ankerite, respectively (Rosenbaum and Sheppard, 1986). CO<sub>2</sub> liberated at 25  
295 °C from calcite was corrected using  $\alpha$  of 1.0014 (Craig, 1957). Carbon and oxygen isotope data are  
296 reported as per mill (‰) deviations relative to Vienna PeeDee belemnite (V-PDB) and Vienna Standard  
297 Mean Ocean Water (V-SMOW), respectively. Lab reproducibility based on complete analysis of  
298 internal standard MAB 2 (Carrara marble) and replicate analyses of calcite unknowns (including acid  
299 digestion at 25 °C) was ± 0.10 ‰ for  $\delta^{13}\text{C}$  and ± 0.12 ‰ for  $\delta^{18}\text{O}$  (1 $\sigma$ ). Reproducibility based on repeat  
300 analysis of dolomite unknowns (including acid digestion at 100 °C) was ± 0.09 ‰ for  $\delta^{13}\text{C}$  and ± 0.10  
301 ‰ for  $\delta^{18}\text{O}$  (1 $\sigma$ ).

302 Pyrite separates were analysed by standard techniques (Robinson and Kusakabe, 1975). SO<sub>2</sub> gas was  
303 liberated by combusting sulfides with excess Cu<sub>2</sub>O at 1075 °C, in vacuo. Liberated SO<sub>2</sub> was analysed  
304 on a VG Isotech SIRA II mass spectrometer, and standard corrections applied to raw  $\delta^{66}\text{SO}_2$  values to  
305 produce  $\delta^{34}\text{S}$ . The data were calibrated using international standards NBS-123 (Sharp, 2017) and IAEA-  
306 S-3 (Mann et al., 2009), and the SUERC standard CP-1. Lab reproducibility was ± 0.3 ‰ (1 $\sigma$ ). Data  
307 are reported in  $\delta^{34}\text{S}$  notation as per mil (‰) deviations from the Vienna Cañon Diablo Troilite (V-CDT)  
308 standard.

309 *Oxygen isotopes in magmatic zircons*- Zircon  $\delta^{18}\text{O}$  values were measured by SHRIMP on 3 samples of  
310 quartz monzodiorite and quartz monzonite from the Falémé Batholith (RG10036, RG10039, RG10050)  
311 and one sample of Bambadji Formation andesitic volcanoclastic rock (RG10030) (Fig. 2). Descriptions  
312 of these rocks and the associated U-Pb zircon geochronology are provided by Allibone et al. (in press).  
313 Oxygen (<sup>18</sup>O/<sup>16</sup>O) isotope ratios were measured for a selection of magmatic areas within zircon grains  
314 in order to characterize the isotopic composition of the magma from which they crystallized and thereby

315 investigate the nature of the source(s) of these magmas. Following the U-Pb analyses, the SHRIMP U-  
316 Pb pits, 1-2  $\mu\text{m}$  deep, were lightly polished away and oxygen isotope analyses were made in exactly the  
317 same location using SHRIMP II fitted with a Cs ion source and an electron gun for charge compensation  
318 as described by Ickert et al. (2008). Oxygen isotope ratios were determined in multiple-collector mode  
319 using an axial continuous electron multiplier (CEM) triplet collector, and two floating heads with  
320 interchangeable CEM - Faraday Cups. The FC1 (Duluth Gabbro) reference zircons were analyzed to  
321 monitor and correct for isotope fractionation. The measured  $^{18}\text{O}/^{16}\text{O}$  ratios and calculated  $\delta^{18}\text{O}$  values  
322 have been normalized relative to a FC1 weighted mean  $\delta^{18}\text{O}$  value of 5.61 ‰ (Fu et al., 2015).  
323 Reproducibility in the FC1 reference zircon  $\delta^{18}\text{O}$  value was  $\pm 0.40$  ‰ ( $2\sigma$  uncertainty) for the analytical  
324 session. Temora 2 reference zircons were analysed in the same session as a secondary reference and  
325 gave a  $\delta^{18}\text{O}$  value of  $8.04 \pm 0.37$  ‰, in agreement with that reported by Ickert et al. (2008).

## 326 **Results**

### 327 *Sulfur isotopes*

328 Sulfur isotope data are listed in full in Table 2. Auriferous sulfides from the Loulo Au deposits and their  
329 satellites have  $\delta^{34}\text{S}$  values between 5.8 and 15.5 ‰, with a mean of 9.6 ‰ ( $n=74$ ) (Fig. 5a) (Fouillac et  
330 al., 1993; Lambert-Smith et al., 2016b; Lawrence et al., 2013b). Diagenetic pyrite from the Kofi series  
331 shows a broad range from 6.4 to 25.1 ‰. New  $\delta^{34}\text{S}$  data (Fig. 5b) from Kabe West ranges from -4.6 to  
332 3.4 ‰ ( $n=9$ ; mean of -0.4 ‰). Sulfides at Baqata range from 5.5 to 11.8 ‰ ( $n=4$ ; mean of 8.1 ‰).  
333 Kolya exhibits  $\delta^{34}\text{S}$  values from 4.2 to 14.2 ‰ ( $n=5$ ; mean of 9 ‰). Mineralization at Boboti ranges  
334 from 1.7 to 3.9 ‰ ( $n=5$ ; mean of 2.5 ‰). Sulfides at the Karakaene Ndi skarn range from 2.8 to 11.9  
335 ‰ ( $n=11$ ; mean of 5.3 ‰) (Fig. 5c). Early sulfides disseminated within the massive Fe ore and hosted  
336 in Fe oxide veins range from 2.8 to 4.4 ‰, whereas late sulfide-rich veins range from 4.9 to 11.9 ‰.

### 337 *Carbon isotopes*

338 Carbon isotope data are listed in full in Table 3. The  $\delta^{13}\text{C}$  values for carbonate country rocks, and barren  
339 and mineralized veins in the Loulo Mining District range from -21.7 to 3.8 ‰ (mean of -7.3 ‰;  $n=79$ ).  
340 The dataset for Au-bearing veins exhibits peaks in  $\delta^{13}\text{C}$  at -10 ‰, -6 ‰ and at 0 ‰ (Fig. 6a). Data from  
341 Kofi Series dolostones provide a local  $\delta^{13}\text{C}$  values for carbonate country rocks. These range from -3.1  
342 to 1.3 ‰ (mean of -0.5 ‰;  $n=10$ ).

343 Sulfidized carbonate-bearing veins in the Kofi Series show a broad range in  $\delta^{13}\text{C}$  values from -21.7 to  
344 -3.7 ‰ ( $n=55$ ) (Fig. 6a). This population is largely unimodal, with a minor negative skew toward lower  
345  $\delta^{13}\text{C}$  values (mode at approximately -8 ‰). The Bambadji exploration targets (Fig. 6b) show a range in  
346  $\delta^{13}\text{C}$  from -16.8 to -3.7 ‰ (mean of -8.4 ‰;  $n=13$ ). Baqata veins range from -15.0 to -3.7 ‰ (mean of  
347 -8.6 ‰;  $n=6$ ). Kolya veins range from -8.8 to -5.1 ‰ (mean of -7.7 ‰;  $n=5$ ). Kabe West ranges from -



348 8.6 to -5.9 ‰ (mean of -7.4 ‰; n=6). Gefa ranges from -16.8 to -7.0 ‰ (mean of -10.2 ‰; n=4). Gara,  
349 Yalea, and Goukoto show the greatest range of values, from -21.7 to -4.5 ‰ (mean of -11.6 ‰; n=32).  
350 Gara shows a range from -14.4 to -4.5 ‰ (mean of -9.6 ‰; n=16), Yalea from -21.7 to -10.6 ‰ (mean  
351 of -16.7 ‰; n=8), and Goukoto from -13.6 to -6.3 ‰ (mean of -9.1 ‰; n=8). In contrast, barren (sulfide  
352 absent) carbonate-bearing hydrothermal veins show a similar population distribution to carbonate  
353 country rocks. This ranges from -2.4 to 3.8 ‰ (mean of -0.7 ‰; n=9) (Fig. 6a). Calcite from sulfide  
354 veins at the Karakaene Ndi skarn deposit range from -4.1 to -1.8 ‰ (n=7; mean of -3.0 ‰) (Fig. 6c).

#### 355 *Oxygen isotopes in carbonates*

356 Oxygen isotope data for carbonate minerals are listed in full in Table 3. The O isotope ratios of  
357 carbonates in the Loulo district exhibit a wide range from 11.4 to 23.3 ‰ (n=79). The data are not  
358 normally distributed and have a positive skew toward higher  $\delta^{18}\text{O}$  values (Fig. 6d). Kofi series  
359 limestones tend to exhibit heavier  $\delta^{18}\text{O}$  values than hydrothermal veining, ranging between 19.1 and  
360 23.3 ‰, with one outlying value at 15.1 ‰ (mean of 20.3 ‰; n=10). Barren hydrothermal veins are  
361 indistinguishable from mineralized hydrothermal veins based on their O-isotopic composition (Fig. 6e).  
362 Barren veins range from 11.7 to 21.1 ‰ (mean of 15.8 ‰; n=14). Mineralized veins range from 11.4  
363 to 23.2 ‰ (mean of 15.6 ‰; n=55). Calcite from sulfide veins at the Karakaene Ndi skarn deposit range  
364 from -12.0 to -13.5 ‰ (n=7; mean of -12.6 ‰) (Fig. 6f).

#### 365 *Oxygen isotopes in magmatic zircons*

366 Oxygen isotope data in magmatic zircons is listed in full in Appendix Table A1. The zircon  $\delta^{18}\text{O}$  values  
367 obtained from Bambadji Formation andesitic volcanoclastic rock sample RG10030 range between 6.4  
368 and  $8.4 \pm 0.5$  ‰ with a weighted mean value of  $7.2 \pm 0.7$  ‰ (MSWD of 13). However, a probability  
369 density plot shows a minor mode at around 6.5 ‰, with scatter among higher values. All grains analysed  
370 have U-Pb isotopic ratios < 10% discordant implying their oxygen isotope ratios are unlikely to have  
371 been markedly affected by post crystallisation Pb-loss ref.

372 Zircons from two samples of the Highway Pluton (RG10036, RG10039) were analysed.. The 5 most  
373 concordant zircon analyses in RG10036 have  $\delta^{18}\text{O}$  ratios of between 7.0 and  $8.4 \pm 0.5$  ‰. The two most  
374 concordant analyses from RG10039 have associated  $\delta^{18}\text{O}$  ratios of 7.0 and  $8.1 \pm 0.5$  ‰, respectively.  
375 Remaining discordant zircons from these two samples have  $\delta^{18}\text{O}$  ratios (6.5 to 8.4 ‰), which are in  
376 broad agreement with the range of values in concordant zircons in all the samples (6.4 to 8.4 ‰) and  
377 may therefore be considered with the other data. The weighted mean for RG10036 is  $7.9 \pm 0.4$  ‰  
378 (MSWD of 8.4). RG10039 has too few analyses to be significant, though the weighted mean of 7.7 ‰  
379 is in broad agreement with data from the other samples. A sample from the Balangouma Pluton, west  
380 of Gara (RG10050), contains relatively abundant concordant zircon whose  $\delta^{18}\text{O}$  ratios range between  
381 6.5 and  $8.1 \pm 0.5$  ‰ with a mean of  $7.6 \pm 0.3$  ‰ (MSWD of 3.8).

382 A weighted mean of all the zircon data yields a  $\delta^{18}\text{O}$  value of  $7.6 \pm 0.2$  with an MSWD of 8.2. However,  
383 a probability density plot of the entire dataset suggests that there are two general values recorded,  
384 with a major mode at : a more prominent value around  $7.9 \pm 0.1$  ‰ and a less prominent lower  
385 value minor mode around  $6.7 \pm 0.2$ ‰.

## 386 Discussion

### 387 *S-isotope Compositions and Sulfur Sources*

388 New  $\delta^{34}\text{S}$  data from the Au occurrences at Kabe West, Baqata, Boboti, and Kolya (-4.6 to 14.2 ‰)  
389 partially overlap the range of values for the Loulo Au deposits (5.8 to 15.5 ‰) and those of diagenetic  
390 pyrite from the Kofi series (6.4 to 25.1 ‰), though they also extend to lower ratios (Fig. 5 a and b).  
391 Lambert-Smith et al. (2016b) interpret these data to indicate that sulfur in the main Loulo Au deposits  
392 is derived from a metasedimentary source. Sulfides at the Karakaene Ndi Fe skarn change from lower  
393 isotopic values in early disseminated sulfides (2.8 to 4.4 ‰), to higher values in late sulfide-rich veins  
394 (4.9 to 11.9 ‰), which overlap with the range of  $\delta^{34}\text{S}$  in Kofi series diagenetic pyrite (Fig. 5c). This  
395 suggests that paragenetically early sulfur in the skarn was dominantly sourced from magmatic fluids  
396 ( $\delta^{34}\text{S} = 0 \pm 2$  ‰) (Ohmoto, 1972), but as the hydrothermal system developed, sulfur with high  $\delta^{34}\text{S}$  (> 4  
397 ‰) was incorporated from the Kofi series metasedimentary rocks or the Bambadji Formation volcanic  
398 rocks. Persistently low  $\delta^{34}\text{S}$  values at the Boboti and Kabe West Au prospects (-4.6 to 3.9 ‰) imply a  
399 magmatic sulfur source.

### 400 *C-isotope Compositions and Carbon Sources*

401 Carbonate minerals from barren hydrothermal veins and dolostone country rocks throughout the  
402 southern Kofi Series have  $\delta^{13}\text{C}$  values between -3.1 ‰ and 3.8 ‰ (Fig. 6a, b), with means of -0.7 and  
403 -0.5 ‰, respectively. These values are typical for Paleoproterozoic marine carbonate (Strauss and  
404 Moore, 1992). This indicates that barren veins likely formed through dissolution of carbonate minerals  
405 in the host sedimentary rocks (Dietrich et al., 1983; Elmer et al., 2006; Lawrence et al., 2013b).  
406 Compositions of auriferous veins in the Kofi Series are more heterogeneous, ranging from -21.7 to -3.7  
407 ‰ (mean of -9.9 ‰) (Fig. 6a, b). The lowest ratios at Yalea (-19.5 to -21.7 ‰) (Lawrence et al., 2013b),  
408 are within the  $\delta^{13}\text{C}$  range of Precambrian organic matter, at  $-24.7 \pm 6$  ‰ (Schidlowski et al., 1975,  
409 Papineau et al., 2010). This is similar to carbonaceous material in of the Paleoproterozoic Kumasi Basin  
410 in Ghana, which yield mean  $\delta^{13}\text{C}_{\text{org}}$  of  $-23 \pm 5$  ‰ (Mumin et al., 1996; Oberthuer et al., 1996). The  $\delta^{13}\text{C}$   
411 of auriferous veins from elsewhere in the Loulo district, including most data from Baqata, Kolya, Kabe  
412 West and Gefa (Fig. 6b), fall between -16 and -4 ‰. These higher values could reflect contributions of  
413 carbon from either (1) the Kofi Series dolostones or (2) magmatic  $\text{CO}_2$  ( $\delta^{13}\text{C}_{\text{CO}_2} \approx -5$  to  $-10$  ‰; Ohmoto,  
414 1972).

415 In either case, the range of compositions indicate a contribution of  $^{13}\text{C}$ -depleted organic carbon to the  
416 hydrothermal system (Fig. 6a). The two most probable mechanisms by which this might occur are: 1)  
417 oxidation of graphite derived from organic matter ( $\text{C} + \text{O}_2 \rightarrow \text{CO}_2$ ), or 2) hydrolysis of graphite ( $2\text{C} +$   
418  $2\text{H}_2\text{O} \rightarrow \text{CO}_2 + \text{CH}_4$ ). Application of isotopic fractionation factors (using the equations of Ohmoto and  
419 Rye, 1979; Golyshev, et al. 1981; Horita, 2001) for average ore forming temperatures in the Loulo  
420 district (ca. 320 °C; Lawrence et al., 2013b; Lambert-Smith et al., 2016b) suggests that *in situ* hydrolysis  
421 of graphite in Kofi dolostones would produce  $\text{CO}_2$  with  $\delta^{13}\text{C} \geq -17.5$  ‰. Carbonate minerals precipitated  
422 from this fluid between 295 and 340 °C (after Lawrence et al 2013b) would have  $\delta^{13}\text{C}$  between of -18.1  
423 and -19.2 ‰. This cannot therefore explain the lowest  $\delta^{13}\text{C}$  values at Yalea. Alternatively, C-isotope  
424 fractionation during hydrolysis could occur in the fluid source region. A fluid with  $X(\text{CO}_2) = 0.2\text{-}0.3$   
425 may be produced at temperatures of 500 to 520 °C at the greenschist-amphibolite transition (Elmer et  
426 al., 2006). This could produce  $\delta^{13}\text{C}_{\text{CO}_2}$  values as low as -20.8 ‰ yielding  $\delta^{13}\text{C}_{\text{dolomite}}$  as low as -21.7 ‰,  
427 depending on the initial  $\delta^{13}\text{C}_{\text{org}}$  of the source material. In both cases we assume open system behaviour,  
428 whereby  $\text{CO}_2$  has undergone significant fractionation from the source graphite composition. This  $^{13}\text{C}$ -  
429 depleted fluid may then have interacted with country rocks in the Kofi Series or a fluid (brine?) of  
430 differing composition, to produce the wide range of observed values.

431 The isotopic compositions of late carbonate-sulfide veining at the Karakaene Ndi Fe skarn deposit (-  
432 4.1 to -1.8 ‰) are  $\sim 1$  ‰ above the expected range of values for a magmatic fluid (Fig. 6c). A cooling  
433 magmatic fluid should precipitate carbonate minerals with lower  $\delta^{13}\text{C}$ ; therefore, it seems likely that  
434 fluid mixing or wall rock interaction have modified the fluid. The most likely scenario is incorporation  
435 of heavier  $\delta^{13}\text{C}$  from the Kofi dolostones during hydrothermal activity around the skarn (Fig. 6a, c).  
436 This is consistent with the interpretation of the  $\delta^{34}\text{S}$  data (Fig. 5a, c).

#### 437 *O-isotope Compositions and Oxygen Sources*

438 The  $\delta^{18}\text{O}$  values in hydrothermal carbonate veins in the Kofi Series are more homogeneous compared  
439 with the  $\delta^{13}\text{C}$  values. Barren, sulfidized and auriferous veins have near identical mean  $\delta^{18}\text{O}$  values of  
440 15.8, 15.0, and 15.6 ‰, respectively, and range from 11.4 to 23.2 ‰ (Fig. 6 d, e, f). Isotopic  
441 compositions above  $\sim 18$  ‰ in auriferous veins are interpreted to represent disequilibrium as  $\delta^{18}\text{O}$  in  
442 paired quartz-dolomite samples at Goukoto and Yalea display  $\delta^{18}\text{O}_{\text{quartz}} < \delta^{18}\text{O}_{\text{dolomite}}$  (Lambert-Smith  
443 et al., 2016b; Lawrence et al., 2013b). This scenario suggests later modification of  $\delta^{18}\text{O}_{\text{dolomite}}$  (Jenkin  
444 et al., 1991). Most samples with  $\delta^{18}\text{O}$  below  $\sim 14$  ‰ are from the western Kofi Au prospects (Fig. 6d  
445 and e), which show relatively high  $\delta^{13}\text{C}$  values  $> -10$  ‰ (Fig. 6b).

446 O-isotope compositions for Falémé batholith magmatic rocks are constrained by  $\delta^{18}\text{O}_{\text{zircon}}$  data obtained  
447 via SHRIMP analysis, the dominant population of which yield a  $\delta^{18}\text{O}_{\text{zircon}}$  value of  $7.9 \pm 0.1$  ‰ (2 SD;  
448  $n=28$ ) (see App. Table A1). We estimated  $\delta^{18}\text{O}_{\text{magma}}$  using melt-zircon fractionation values of Trail et

449 al. (2009) ( $\Delta_{\text{melt-zircon}}$  at 800 °C = 1.7 ‰). We then applied the plagioclase-water fractionation values of  
 450 Zheng (1993) ( $\Delta_{\text{albite-H}_2\text{O}}$  at 700 °C = 0.2 ‰), to calculate a  $\delta^{18}\text{O}_{\text{H}_2\text{O}}$  value of 9.4 ‰ for the Falémé  
 451 batholith. Zircon crystallisation temperatures were estimated using data in Samperton et al. (2017). The  
 452 maximum range of  $\delta^{18}\text{O}_{\text{H}_2\text{O}}$  values for a magmatic-hydrothermal fluid exsolved from the Falémé  
 453 batholith is 7.9 to 10.0 ‰. The average  $\delta^{18}\text{O}_{\text{fluid}}$  value calculated from carbonates in the Loulo district  
 454 overlaps this range at  $10.2 \pm 2.3$  ‰ (calculated at 320 °C using the equations of Zheng, 1999). However,  
 455 these data alone cannot constrain the fluid source as  $\delta^{18}\text{O}_{\text{fluid}}$  values for local magmatic and metamorphic  
 456 water (~4 to 25 ‰) overlap (Sheppard, 1986). At best these data are permissive of either, or both, fluid  
 457 sources, and so must be interpreted in their geological context, together with  $\delta^{13}\text{C}$  data. The western  
 458 Kofi Au prospects have lower average  $\delta^{18}\text{O}_{\text{fluid}}$  values of 9.1 ‰ (Baqata), 8.6 ‰ (Kolya), 8.3 ‰ (Kabe  
 459 West), and 8.5 ‰ (Gefa), whereas the intrusive-hosted Boboti target has a significantly lower value of  
 460 6.6 ‰. These lower values suggest the involvement of fluids sourced from the Falémé batholith in Au  
 461 mineralization at these locations. Similarly,  $\delta^{18}\text{O}_{\text{calcite}}$  at Karakaene Ndi, at temperatures of 550 °C, yield  
 462 a  $\delta^{18}\text{O}_{\text{fluid}}$  range from 9.6 to 11.1 ‰, overlapping the upper end of local magmatic water values.

#### 463 *Carbon-Oxygen Isotope Modelling*

464 To test whether magmatic fluids may have contributed to the Au-bearing hydrothermal system of the  
 465 Loulo district, we calculated the C-O isotope compositions of mixtures between a dilute metamorphic  
 466 aqueous-carbonic fluid, and 1) a hypersaline brine derived from metaevaporites, and 2) a magmatic  
 467 hydrothermal fluid sourced from the Falémé batholith. The equations of Schwinn et al. (2006) were  
 468 used to calculate  $\delta^{13}\text{C}$  values for carbonates precipitated from a mixed fluid ( $\delta^{13}\text{C}_M$ ):

$$469 \quad \delta^{13}\text{C}_M = \left( \frac{m_B^* f_B}{m_B^* f_B + m_{AC}^* (1 - f_B)} \right) \cdot \delta^{13}\text{C}_B + \left( \frac{m_{AC}^* (1 - f_B)}{m_B^* f_B + m_{AC}^* (1 - f_B)} \right) \cdot \delta^{13}\text{C}_{AC}$$

470 Where  $\delta^{13}\text{C}_B$ ,  $\delta^{13}\text{C}_{AC}$ , and represent C-isotope compositions for the brine, the aqueous-carbonic fluid,  
 471 respectively. The molalities of carbon in the brine  $m_B^*$  and aqueous-carbonic fluid  $m_{AC}^*$ , have been  
 472 calculated using the following equation:

$$473 \quad m_B^* = \frac{m_B}{(n_W + \sum m_{i,B})}$$

474 where  $n_w$  is the total number of moles  $\text{H}_2\text{O}$  in 1 kg water,  $m_B$  is the uncorrected molality of carbon in  
 475 the brine, and  $\sum m_{i,B}$  is the sum of the molalities of all solutes in the brine. This approach considers the  
 476 significant salinity differences between the two fluids by correcting for total solute concentrations  
 477 (Schwinn et al., 2006). These equations were adapted to model  $\delta^{18}\text{O}_{\text{fluid}}$ .

478 End member fluid isotopic and chemical compositions are detailed in Table 4. The starting isotopic  
 479 composition for the brine ( $\delta^{13}\text{C}_{\text{fluid}} = 1.8$  ‰ and  $\delta^{18}\text{O}_{\text{fluid}} = 17.3$  ‰) is based on devolatilization of a

480 dolostone with similar initial  $\delta^{13}\text{C}$  and  $\delta^{18}\text{O}$  to that of Kofi Series dolostones (Valley, 1986). Starting  
 481 compositions of the magmatic fluid ( $\delta^{13}\text{C}_{\text{fluid}} = -6.0 \text{ ‰}$  and  $\delta^{18}\text{O}_{\text{fluid}} = 9.4 \text{ ‰}$ ) are based upon  $\delta^{18}\text{O}_{\text{H}_2\text{O}}$   
 482 from the Falémé batholith (App. Table A1) and the accepted range of magmatic  $\delta^{13}\text{C}_{\text{CO}_2}$  (Taylor, 1974).  
 483 The aqueous-carbonic fluid is assumed to have the composition  $\delta^{13}\text{C}_{\text{fluid}} = -27.0 \text{ ‰}$  and  $\delta^{18}\text{O}_{\text{fluid}} = 10.2$   
 484  $\text{‰}$ . This represents a fluid derived from metamorphic devolatilization of  $\text{C}_{\text{org}}$  bearing sediments.  $\delta^{13}\text{C}$   
 485 and  $\delta^{18}\text{O}$  of dolomite were calculated at ore forming temperatures of 320 °C.

486 Figure 7 shows that the isotopic character of auriferous hydrothermal veins at Loulo cannot be explained  
 487 by binary mixing between end members of metamorphic aqueous-carbonic fluid and either a meta-  
 488 evaporite derived brine, or a magmatic fluid from the Falémé batholith. We note above that the isotopic  
 489 signature of the unequivocally magmatic Karakaene Ndi skarn does not correspond directly to Falémé  
 490 magmatic fluid values. This suggests that any magmatic-hydrothermal fluid in even the most proximal  
 491 parts of the hydrothermal system may be somewhat cryptic. We have therefore modelled the effects of  
 492 water-rock reaction on the C-O isotope system (Fig. 7), with the objectives of (1) explaining the  $\delta^{13}\text{C}$   
 493 and  $\delta^{18}\text{O}$  signature of the Karakaene Ndi skarn and (2) investigating the magmatic contributions to the  
 494 Loulo Au deposits, particularly the prospects in the western Kofi Series. This was accomplished using  
 495 the following equation, assuming open system behaviour (modified after Shelton, 1983):

$$496 \quad \delta_r^f = (\delta_r^i - \delta_w^i + \Delta) e^{\frac{-Wc_w}{Rc_r}} + \delta_w^i - \Delta$$

497 Where  $_r$  and  $_w$  denote rock and water (or mineral and fluid), respectively.  $\delta^i$  and  $\delta^f$  denote the initial  
 498 and final isotopic composition, respectively.  $\Delta$  is the fluid-mineral per mil fractionation as a function of  
 499 temperature (in this case 320 °C for the metamorphic fluid and 550 °C for the magmatic-hydrothermal  
 500 fluid).  $C$  indicates concentration,  $R$  mass of rock, and  $W$  mass of water. The reaction curves were  
 501 modelled for water-rock ratios between 100 and 0.01. The metamorphic fluid was modelled at  $\text{XCO}_2$   
 502 = 0.2, and the magmatic-hydrothermal fluid at 0.11 (Lambert-Smith et al., 2016b, Lawrence et al.,  
 503 2013b). End member fluid isotopic and chemical compositions are as detailed above (Table 4). Average  
 504 Kofi dolostone compositions were used for the host rock.

#### 505 *Interactions between the Loulo and Falémé Mineral Systems*

506 Carbonate veins from Karakaene Ndi fall along water-rock reaction pathways typical of magmatic-  
 507 hydrothermal systems (Fig. 7) (e.g. Pass et al., 2014). These data represent a hot (~550 °C) magmatic  
 508 fluid from the Falémé Batholith interacting with significantly cooler carbonate-rich wall rocks with high  
 509  $\delta^{13}\text{C}$ . This pattern is replicated in  $\delta^{34}\text{S}$  data (Fig. 5c), where a shift to higher  $\delta^{34}\text{S}$  in later veins suggests  
 510 an influx of wall rock sulfur as the hydrothermal system began to cool and retrograde skarn  
 511 mineralization began.

512 C-O isotope modelling indicates that water-rock reaction between a metamorphic fluid and carbonate-  
513 rich Kofi Series host rocks was an important process at Gara, Yalea and Goukoto and can partly  
514 explain the C and O isotopic compositions of these deposits (Fig. 7). Critically, the three world class  
515 deposits at Loulo show limited isotopic evidence for direct contribution of magmatic volatiles, with the  
516 possible exception of Gara (Fig. 7). In contrast, the Au prospects in the western Kofi Series at Baqata,  
517 Kolya, Kabe West and Gefa (as well as limited data points from Gara) have higher  $\delta^{13}\text{C}$  and lower  $\delta^{18}\text{O}$   
518 values than the main Loulo deposits, which fall between the aqueous carbonic fluid-dolostone and  
519 magmatic brine-dolostone reaction curves (Fig. 7).

520 On the basis of these data, we suggest that mineralization in the small Au prospects adjacent to the  
521 margin of the Falémé Batholith was deposited from a mixed aqueous-carbonic and magmatic fluid, both  
522 of which had been modified through reaction with Kofi Series dolostone and/or Bambadji Formation  
523 volcanic rocks prior to mixing. While isotopic values for the Kolya, Baqata and Gefa prospects are  
524 largely in agreement with those of the main Loulo Au deposits, including their low  $\delta^{34}\text{S}$  values (Fig. 5a,  
525 b), those for Kabe West and Boboti plot at lower  $\delta^{18}\text{O}$ , implying a stronger magmatic-hydrothermal  
526 affinity (Fig. 6b and 7). Kabe West and Boboti are both hosted within intensely albitized igneous rocks  
527 on the margin of the Falémé batholith, which is intruded by multiple generations of small-scale dikes  
528 and stocks consistent with an elevated contribution of magmatic volatiles. Furthermore, low  $\delta^{18}\text{O}$  values  
529 at Baqata, Kolya, and Gefa are consistent with the presence of thin diorite dikes within 5 m of  
530 mineralization (Lambert-Smith, 2014a). These dikes may have exsolved small aliquots of magmatic-  
531 hydrothermal fluid similar to those responsible for skarn alteration, resulting in the heterogeneous  
532 isotopic signature of Au prospects in the western Kofi Series. It should also be noted that some of the  
533 isotopic values for hydrothermal minerals in the western Kofi Au prospects could be generated simply  
534 from a cooling end-member magmatic fluid.

### 535 *Metallogenic Model for the Loulo District*

536 Lambert-Smith et al. (2016c) reported that pre-ore hydrothermal tourmalines at Gara and Yalea North  
537 were deposited from an  $^{11}\text{B}$ -rich fluid whose isotopic character was comparable with metaevaporite  
538 source rocks. While evaporite beds have not been identified in the Kofi series, the B-isotope data  
539 suggest the marly dolostones in the west of the Kofi basin may have contained evaporitic horizons (Fig.  
540 8a). The Falémé batholith intruded these marly dolostones and evaporite horizons (Fig. 2) between  $2084$   
541  $\pm 8$  Ma and  $2070 \pm 5$  Ma, during which time the Falémé skarns also formed (Fig. 8 b and c). Field  
542 relationships between albitization and magmatic rocks in the Kofi Series suggest NaCl,  $\text{CO}_2$  and B were  
543 initially mobilized during syn- $D_1$  metamorphism of Kofi Series dolostones, before Falémé magmatism,  
544 giving rise to a paragenetically early brine and widespread associated albitic and tourmaline alteration.  
545 Falémé magmatism now seems likely to have contributed both heat and magmatic-hydrothermal fluid  
546 to this evolving system, synchronous with on-going  $D_2$  metamorphism and minor transcurrent

547 deformation. These magmatic fluids may have evolved into high temperature saline brines through  
548 reaction with the dolostones or mixing with a metamorphic brine derived from earlier devolatilization  
549 of the dolostones and interbedded evaporites. This scenario would explain both the high fluid  
550 temperatures (>400 °C) documented by Lawrence et al. (2013b) and the meta-evaporite B-isotope  
551 signature described by Lambert-Smith et al. (2016c), as it seems likely that the dominant B reservoir in  
552 such a scenario would be the evaporative wall rocks.. High thermal gradients and permissive structural  
553 architecture allowed widespread circulation of this hybrid magmatic-hydrothermal and meta-evaporitic  
554 brine, resulting in on-going, multi-phase, district-scale Na and B metasomatism prior to and during Au  
555 mineralization (Lawrence et al., 2013b; Lambert-Smith et al., 2016a; Lambert-Smith et al., 2016b;  
556 Lambert-Smith et al., 2016c) (Fig. 8b). At the Karakaene Ndi skarn high  $\delta^{34}\text{S}$  and  $\delta^{13}\text{C}$  values suggest  
557 a contribution to the hydrothermal system from wall rocks with isotopic characteristics similar to the  
558 Kofi dolostones. Similarly, at Gara a shift from high  $\delta^{11}\text{B}$  (~12.7 ‰) to lower values (~5 ‰) indicates  
559 that in places, brines containing both evaporite and magmatic components (hybrid) mixed with more  
560 dilute aqueous-carbonic fluids during Au mineralization (Lambert-Smith et al., 2016c). This implies  
561 that the hybrid brine contributed to the formation of both the Falémé skarns and the Loulo Au deposits.

562 Given that the aqueous-carbonic fluid is present in all Au deposits in the Loulo region, whereas the  
563 hypersaline brine is absent at Yalea, it seems likely that the former was more important in terms of  
564 introducing Au to the system. Stable isotope data from Au-related pyrite and arsenopyrite ( $\delta^{34}\text{S}$  5.8 to  
565 9.6 ‰), quartz ( $\delta^{18}\text{O}$  15.8 to 16.3 ‰ yielding a mean  $\delta^{18}\text{O}_{\text{fluid}}$  of approx. 9.7 ‰ at 320 °C), dolomite  
566 ( $\delta^{13}\text{C}$  -15.8 to -21.7 ‰) (Lawrence et al., 2013b) and tourmaline ( $\delta^{11}\text{B}$  -0.5 to 9.3 ‰) (Lambert-Smith  
567 et al., 2016c) at Yalea are all compatible with the aqueous-carbonic fluid being sourced from Kofi Series  
568 siliciclastic metasedimentary and carbonate rocks (Rye and Ohmoto, 1974; Sheppard, 1986; van  
569 Hinsberg et al., 2011) with a significant organic C component (Schidlowski et al., 1975). Our new data  
570 and modelling show that the brine with which the aqueous-carbonic fluid mixed is likely to have  
571 evolved from interaction between magmatic-hydrothermal fluid(s) and the Kofi Series dolostones ( $\pm$   
572 meta-evaporites). Heat from the intrusion of the Falémé Batholith could conceivably have perturbed the  
573 local geothermal gradient sufficiently to drive this district scale hydrothermal system.

#### 574 *Implications for Orogenic Au and other Hydrothermal Systems*

575 Our data suggest that magmatic fluids can make a significant contribution to some orogenic Au  
576 mineralization. In the Loulo example magmatism, combined with highly reactive dolostone and  
577 evaporitic country rocks resulted in generation of a hybrid brine that appears to have acted as a chemical  
578 trap for this and other aqueous carbonic Au-bearing fluids.

579 Comparisons between the Loulo District and some iron oxide Cu-Au (IOCG) provinces are also  
580 instructive. Deposits of the Carajás Mineral Province of northern Brazil are somewhat analogous in that  
581 they feature hypersaline brines (up to 58 wt. % equiv. NaCl) (da Costa Silva et al., 2015), which have

582 derived their salt content from meta-evaporitic rocks (Xavier et al., 2008; Riehl and Cabral, 2018).  
583 Intrusion of magma into evaporite bearing rocks has set up district-scale hydrothermal systems resulting  
584 in abundant sodic and calcic alteration. Schwartz and Melcher (2004) and Lawrence et al. (2013a) have  
585 both suggested that the Falémé skarns share characteristics with IOCG deposits. Notably, the skarns are  
586 rich in low-Ti iron oxides and are associated with widespread and paragenetically early alteration  
587 associated with both CO<sub>2</sub>-rich and saline fluids. The Falémé skarns however, differ in that they contain  
588 no economic Cu, only relatively low-grade Au, and are more intimately associated with magmatic rocks  
589 than is typical for IOCG deposits (c.f. Williams et al., 2005).

590 The isotopic data largely supports a metamorphic devolatilization model for the system at Loulo (e.g.  
591 Groves et al., 2019). Though the term may not be wholly appropriate in describing the Loulo deposits,  
592 there is a clear metamorphic signature in the isotope data with deposits such as Yalea formed largely  
593 without the influence of the hybrid magmatic-hydrothermal/evaporite-derived brine.

594

### Conclusions

595 Taken together, our data suggest a critical role for magmatism in the development of early alteration  
596 assemblages in the Loulo District, in the genesis of the Falémé iron skarns, and in those Au deposits  
597 that formed in response to fluid mixing. In these deposits, including Gara and the minor Au occurrences  
598 in close spatial association with dikes and sills on the margin of the Falémé Batholith, there is strong  
599 indications that evolved magmatic fluids were present during mineralization.

600 We envisage a scenario where the Falémé Batholith intrudes the marly evaporite-bearing carbonate  
601 rocks of the western Kofi Series. Fluids exsolved from the Falémé Batholith interacted with the marly  
602 dolostones generating a hypersaline brine which circulated through the Kofi and Falémé lithologies.  
603 This resulted in the widespread albitization and tourmalinization characteristic of the region, which  
604 hardens certain lithologies providing a favourable competency contrast for Au-bearing fluids to exploit.  
605 Early metasomatism is overprinted by orogenic-style Au and Fe skarn mineralization; the former related  
606 to the incursion of aqueous-carbonic fluids. These fluids largely precipitate minerals due to pressure  
607 fluctuations or water-rock reactions (Lambert-Smith et al., 2016b, Lawrence et al., 2013b), but in places  
608 partially mix with the magmatic-evaporitic brines which provide a chemical trap for Au mineralization.  
609 In this way, the intrusion of the Falémé Batholith played a direct role in the development of the Loulo  
610 Au mineral system. Skarn formation is likely to have been promoted by the presence of Cl-rich brines,  
611 which would have encouraged metal transport in FeCl<sub>2</sub> complexes.

### 612 Acknowledgements

613 This research was funded by Randgold Resources and Kingston University. Isotopic analyses were  
614 carried out through a NERC Facilities Grant (IP-1252-0511). A. J. Boyce is funded by NERC support



615 to the Isotope Community Support Facility at SUERC. The authors wish to thank the technical staff at  
616 SUERC and Kingston for their assistance in carrying out sample preparation and analysis. SHRIMP  
617 zircon oxygen isotope data was acquired by Mark Fanning using the facilities at the Australian National  
618 University as part of a collaborative program funded by Randgold Resources Ltd during 2014-2015.  
619 We also wish to thank Larry Meinert and two anonymous reviewers for their constructive reviews,  
620 which undoubtedly improved the manuscript.

## 621 **References**

- 622 Allibone, A., Teasdale, J., Cameron, G., Etheridge, M., Uttley, P., Soboh, A., Appiah-Kubi, J., Adanu, A.,  
623 Arthur, R. and Mamphey, J., 2002, Timing and structural controls on gold mineralization at  
624 the Bogoso gold mine, Ghana, West Africa: *Economic Geology*, v. 97, p. 949-969.
- 625 Allibone, A., Lawrence, D., Scott, J., Fanning, M., Lambert-Smith, J., Harbidge, R., Vargas, C., Turnbull,  
626 R., Joel Holliday, J., Paleoproterozoic gold deposits of the Loulo district, western Mali:  
627 Society of Economic Geologists Special Publication 23, 2020, in press.
- 628 Baratoux, L., Metelka, V., Naba, S., Jessell, M. W., Grégoire, M. and Ganne, J., 2011, Juvenile  
629 Paleoproterozoic crust evolution during the Eburnean orogeny (~ 2.2–2.0 Ga), western  
630 Burkina Faso: *Precambrian Research*, v. 191, p. 18-45.
- 631 Block, S., Ganne, J., Baratoux, L., Zeh, A., Parra-Avila, L., Jessell, M., Ailleres, L. and Siebenaller, L.,  
632 2015, Petrological and geochronological constraints on lower crust exhumation during  
633 Paleoproterozoic (Eburnean) orogeny, NW Ghana, West African Craton: *Journal of*  
634 *Metamorphic Geology*, v. 33, p. 463-494.
- 635 Campbell Mccuaig, T. and Kerrich, R., 1998, P—T—t—deformation—fluid characteristics of lode gold  
636 deposits: evidence from alteration systematics. *Ore Geology Reviews*, v. 12, p. 381-453.
- 637 Craig, H. 1957, Isotopic standards for carbon and oxygen and correction factors for mass-  
638 spectrometric analysis of carbon dioxide: *Geochimica et cosmochimica acta*, v. 12, p. 133-  
639 149.
- 640 Da Costa Silva, A. R., Villas, R. N. N., Lafon, J.-M., Craveiro, G. S. and Ferreira, V. P., 2015, Stable  
641 isotope systematics and fluid inclusion studies in the Cu–Au Visconde deposit, Carajás  
642 Mineral Province, Brazil: implications for fluid source generation: *Mineralium Deposita*, v.  
643 50, p. 547-569.
- 644 Davis, D., Hirdes, W., Schaltegger, U. and Nunoo, E., 1994, U-Pb age constraints on deposition and  
645 provenance of Birimian and gold-bearing Tarkwaian sediments in Ghana, West Africa:  
646 *Precambrian Research*, v. 67, p. 89-107.
- 647 De Kock, G., Armstrong, R., Siegfried, H. and Thomas, E., 2011, Geochronology of the Birim  
648 Supergroup of the West African craton in the Wa-Bolé region of west-central Ghana:  
649 Implications for the stratigraphic framework: *Journal of African Earth Sciences*, v. 59, p. 1-40.
- 650 Dia, A., Van Schmus, W. and Kröner, A., 1997, Isotopic constraints on the age and formation of a  
651 Palaeoproterozoic volcanic arc complex in the Kedougou Inlier, eastern Senegal, West Africa:  
652 *Journal of African Earth Sciences*, v. 24, p. 197-213.
- 653 Dietrich, D., Mckenzie, J. A. and Song, H., 1983, Origin of calcite in syntectonic veins as determined  
654 from carbon-isotope ratios: *Geology*, v. 11, p. 547-551.
- 655 Eglinger, A., Thébaud, N., Zeh, A., Davis, J., Miller, J., Parra-Avila, L. A., Loucks, R., Mccuaig, C. and  
656 Belousova, E., 2017, New insights into the crustal growth of the Paleoproterozoic margin of  
657 the Archean Kéména-Man domain, West African craton (Guinea): Implications for gold  
658 mineral system: *Precambrian Research*, v. 292, p. 258-289.
- 659 Eichmann, R. and Schidlowski, M., 1975, Isotopic fractionation between coexisting organic carbon—  
660 carbonate pairs in Precambrian sediments: *Geochimica et Cosmochimica Acta*, v. 39, p. 585-  
661 595.

662 Elmer, F., White, R. and Powell, R., 2006, Devolatilization of metabasic rocks during greenschist–  
663 amphibolite facies metamorphism: *Journal of Metamorphic Geology*, v. 24, p. 497-513.

664 Fontaine, A., Eglinger, A., Ada, K., André-Mayer, A.-S., Reisberg, L., Siebenaller, L., Le Mignot, E.,  
665 Ganne, J. and Poujol, M., 2017, Geology of the world-class Kiaka polyphase gold deposit,  
666 West African Craton, Burkina Faso: *Journal of African Earth Sciences*, v. 126, p. 96-122.

667 Fougereuse, D., Micklethwaite, S., Ulrich, S., Miller, J., Godel, B., Adams, D. T. and Mccuaig, T. C.,  
668 2017, Evidence for two stages of mineralization in West Africa’s largest gold deposit: Obuasi,  
669 Ghana: *Economic Geology*, v. 112, p. 3-22.

670 Fouillac, A., Dommaget, A. and Milési, J., 1993, A carbon, oxygen, hydrogen and sulfur isotopic  
671 study of the gold mineralization at Loulo, Mali. *Chemical geology*, v. 106, p. 47-62.

672 Frimmel, H. E. and Hennigh, Q., 2015, First whiffs of atmospheric oxygen triggered onset of crustal  
673 gold cycle: *Mineralium Deposita*, v. 50, p. 5-23.

674 Fu, B., Bröcker, M., Ireland, T.R., Holden, P., and Kinsley, L., 2015, Zircon U-Pb, O, and Hf isotopic  
675 constraints on Mesozoic magmatism in the Cyclades, Aegean Sea, Greece: *Geologische  
676 Rundschau*, v. 104, p. 75–87.

677 Gaboury, D., 2013, Does gold in orogenic deposits come from pyrite in deeply buried carbon-rich  
678 sediments?: Insight from volatiles in fluid inclusions: *Geology*, v. 41, p. 1207-1210.

679 Ganne, J., De Andrade, V., Weinberg, R. F., Vidal, O., Dubacq, B., Kagambega, N., Naba, S., Baratoux,  
680 L., Jessell, M. and Allibon, J., 2011, Modern-Style Plate Subduction Preserved In The  
681 Palaeoproterozoic West African Craton: *Nature Geoscience*, v. 5, p. 60.

682 Goldfarb, R. J., André-Mayer, A.-S., Jowitt, S. M. and Mudd, G. M., 2017, West Africa: The world’s  
683 premier Paleoproterozoic gold province: *Economic Geology*, v. 112, p. 123-143.

684 Goldfarb, R. J. and Groves, D. I., 2015, Orogenic gold: Common or evolving fluid and metal sources  
685 through time: *Lithos*, v. 233, p. 2-26.

686 Goldfarb, R. J., Newberry, R. J., Pickthorn, W. J. and Gent, C. A., 1991, Oxygen, hydrogen, and sulfur  
687 isotope studies in the Juneau gold belt, southeastern Alaska; constraints on the origin of  
688 hydrothermal fluids: *Economic geology*, v. 86, p. 66-80.

689 Golyshev, S.I., Padalko, N.L. and Pechenkin, S.A., 1981, Fractionation of stable oxygen and carbon  
690 isotopes in carbonate systems: *Geochemistry International* v. 18, p. 85-99.

691 Grenholm, M., Jessell, M. and Thébaud, N., 2019, A geodynamic model for the Paleoproterozoic (ca.  
692 2.27–1.96 Ga) Birimian Orogen of the southern West African Craton—Insights into an  
693 evolving accretionary-collisional orogenic system: *Earth-Science Reviews*, v. 192, p. 138-193

694 Groves, D. I., Goldfarb, R. J., Gebre-Mariam, M., Hagemann, S. and Robert, F., 1998, Orogenic gold  
695 deposits: a proposed classification in the context of their crustal distribution and relationship  
696 to other gold deposit types: *Ore geology reviews*, v. 13, p. 7-27.

697 Groves, D. I., Santosh, M., Deng, J., Wang, Q., Yang, L. and Zhang, L., 2019, A holistic model for the  
698 origin of orogenic gold deposits and its implications for exploration: *Mineralium Deposita*,  
699 pp. 1-18.

700 Gueye, M., Siegesmund, S., Wemmer, K., Pawlig, S., Drobe, M., Nolte, N. and Layer, P., 2007, New  
701 evidences for an early Birimian evolution in the West African Craton: An example from the  
702 Kedougou-Kenieba inlier, southeast Senegal: *South African Journal of Geology*, v. 110, p.  
703 511-534.

704 Hein, K. A., 2010, Succession of structural events in the Goren greenstone belt (Burkina Faso):  
705 implications for West African tectonics: *Journal of African Earth Sciences*, 56, p. 83-94.

706 Henley, R.W., Norris, R.J., and Paterson, C.J., 1976, Multistage ore genesis in the New Zealand  
707 Geosyncline: a history of post-metamorphic lode emplacement: *Mineralium Deposita*, v. 11,  
708 p. 180-196.

709 Hirdes, W. and Davis, D., 2002, U–Pb geochronology of paleoproterozoic rocks in the southern part  
710 of the Kedougou-Kenieba Inlier, Senegal, West Africa: evidence for diachronous accretionary  
711 development of the Eburnean province: *Precambrian Research*, v. 118, p. 83-99.

712 Horita, J., 2001. Carbon isotope exchange in the system CO<sub>2</sub>-CH<sub>4</sub> at elevated temperatures:  
713 *Geochimica et Cosmochimica Acta*, v. 65, p. 1907-1919.

714 Ickert, R.B., Hiess, J., Williams, I.S., Holden, P., Ireland, T.R., Lanc, P., Schram, N., Foster, J.J. and  
715 Clement, S.W., 2008, Determining high precision, in situ, oxygen isotope ratios with a  
716 SHRIMP II: Analyses of MPI-DING silicate-glass reference materials and zircon from  
717 contrasting granites: *Chemical Geology* v. 257, p. 114-128.

718 Jenkin, G. R. T., Linklater, C. and Fallick, A. E., 1991, Modeling of mineral  $\delta^{18}\text{O}$  values in an igneous  
719 aureole: Closed-system model predicts apparent open-system  $\delta^{18}\text{O}$  values: *Geology*, v. 19,  
720 p. 1185-1188.

721 John, T., Klemd, R., Hirdes, W. and Loh, G., 1999, The metamorphic evolution of the  
722 paleoproterozoic (Birimian) volcanic Ashanti belt (Ghana, West Africa): *Precambrian*  
723 *Research*, 98, p. 11-30.

724 Kerrich, R. and Wyman, D., 1990, Geodynamic setting of mesothermal gold deposits: An association  
725 with accretionary tectonic regimes: *Geology*, v. 18, p. 882-885.

726 Lambert-Smith, J. S., 2014, The geology, structure and metallogenesis of the world class Loulo-  
727 Bambadji Au district in Mali and Senegal, West Africa: Unpublished Ph.D. thesis, Kingston  
728 upon Thames, UK, Kingston University London, 354 p.

729 Lambert-Smith, J. S., Lawrence, D. M., Müller, W. and Treloar, P. J., 2016a, Palaeotectonic setting of  
730 the south-eastern Kédougou-Kéniéba Inlier, West Africa: New insights from igneous trace  
731 element geochemistry and U-Pb zircon ages: *Precambrian Research*, v. 274, p. 110-135.

732 Lambert-Smith, J. S., Lawrence, D. M., Vargas, C. A., Boyce, A. J., Treloar, P. J. and Herbert, S., 2016b,  
733 The Gounkoto Au deposit, West Africa: Constraints on ore genesis and volatile sources from  
734 petrological, fluid inclusion and stable isotope data: *Ore Geology Reviews*, v. 78, p. 606-622.

735 Lambert-Smith, J. S., Rocholl, A., Treloar, P. J. and Lawrence, D. M., 2016c, Discriminating fluid  
736 source regions in orogenic gold deposits using B-isotopes: *Geochimica et Cosmochimica*  
737 *Acta*, v. 194, p. 57-76.

738 Lawrence, D. M., Lambert-Smith, J. S. and Treloar, P. J., 2016, A Review of Gold Mineralization in  
739 Mali, In Bouabdellah, M. and Slack, J. F. (eds.) *Mineral Deposits of North Africa*. Springer  
740 International Publishing. pp. 327-352.

741 Lawrence, D. M., Treloar, P. J., Rankin, A. H., Harbidge, P. and Holliday, J., 2013a, The geology and  
742 mineralogy of the Loulo mining district, Mali, West Africa: Evidence for two distinct styles of  
743 orogenic gold mineralization: *Economic Geology*, v. 108, p. 199-227.

744 Lawrence, D. M., Treloar, P. J., Rankin, A. H., Boyce, A. and Harbidge, P., 2013b, A fluid inclusion and  
745 stable isotope study at the Loulo mining district, Mali, West Africa: Implications for multifluid  
746 sources in the generation of orogenic gold deposits: *Economic Geology*, v. 108, p. 229-257.

747 Lebrun, E., Thébaud, N., Miller, J., Ulrich, S., Bourget, J. and Terblanche, O., 2016, Geochronology  
748 and lithostratigraphy of the Siguiri district: Implications for gold mineralisation in the Siguiri  
749 Basin (Guinea, West Africa): *Precambrian Research*, v. 274, p. 136-160.

750 Loh, G., Hirdes, W., Anani, C., Davis, D. W. and Vetter, U. K., 2000, Explanatory Notes for the  
751 Geological Map of-Southwest Ghana 1: 100,000-Sekondi (0402A) and Axim (0403B) Sheets.

752 Mcfarlane, H. B., Ailleres, L., Betts, P., Ganne, J., Baratoux, L., Jessell, M. W., and Block, S., 2019,  
753 Episodic collisional orogenesis and lower crust exhumation during the Palaeoproterozoic  
754 Eburnean Orogeny: Evidence from the Sefwi Greenstone Belt, West African Craton:  
755 *Precambrian Research*, v. 325, p. 88-110.

756 Mann, J. L., Vocke Jr, R. D. and Kelly, W. R., 2009, Revised  $\delta^{34}\text{S}$  reference values for IAEA sulfur  
757 isotope reference materials S-2 and S-3: *Rapid Communications in Mass Spectrometry: An*  
758 *International Journal Devoted to the Rapid Dissemination of Up-to-the-Minute Research in*  
759 *Mass Spectrometry*, v. 23, p. 1116-1124.

760 Markwitz, V., Hein, K. A. A., Jessell, M. W. and Miller, J., 2016, Metallogenic portfolio of the West  
761 Africa craton: *Ore Geology Reviews*, v. 78, p. 558-563.

762 Masurel, Q., Thébaud, N., Miller, J. and Ulrich, S., 2017a, The tectono-magmatic framework to gold  
763 mineralisation in the Sadiola-Yatela gold camp and implications for the paleotectonic setting  
764 of the Kédougou-Kéniéba inlier, West Africa: *Precambrian Research*, v. 292, p. 35-56.

765 Masurel, Q., Thébaud, N., Miller, J., Ulrich, S., Hein, K. A., Cameron, G., Béziat, D., Bruguier, O. and  
766 Davis, J. A., 2017b, Sadiola Hill: A world-class carbonate-hosted gold deposit in Mali, West  
767 Africa: *Economic Geology*, v. 112, p. 23-47.

768 Masurel, Q., Thébaud, N., Miller, J., Ulrich, S., Roberts, M. P. and Béziat, D., 2017c, The Alamoutala  
769 Carbonate-Hosted Gold Deposit, Kédougou-Kéniéba Inlier, West Africa: *Economic Geology*, v.  
770 112, p. 49-72.

771 Mcfarlane, C. R., Mavrogenes, J., Lentz, D., King, K., Allibone, A. and Holcombe, R., 2011, Geology  
772 and intrusion-related affinity of the Morila gold mine, southeast Mali: *Economic Geology*, v.  
773 106, p. 727-750.

774 Mumin, A., Fleet, M. and Longstaffe, F., 1996, Evolution of hydrothermal fluids in the Ashanti gold  
775 belt, Ghana; stable isotope geochemistry of carbonates, graphite, and quartz: *Economic  
776 Geology*, v. 91, p. 135-148.

777 Norris, R.J. and Henley, R.W., 1976, Dewatering of a metamorphic pile. *Geology*, v. 4, p. 333-336.

778 Oberthuer, T., Mumm, A. S., Vetter, U., Simon, K. and Amanor, J. A., 1996, Gold mineralization in the  
779 Ashanti Belt of Ghana; genetic constraints of the stable isotope geochemistry: *Economic  
780 Geology*, v. 91, p. 289-301.

781 Oberthür, T., Vetter, U., Davis, D. W. and Amanor, J. A., 1998, Age constraints on gold mineralization  
782 and Paleoproterozoic crustal evolution in the Ashanti belt of southern Ghana: *Precambrian  
783 Research*, v. 89, p. 129-143.

784 Ohmoto, H., 1972, Systematics of sulfur and carbon isotopes in hydrothermal ore deposits: *Economic  
785 Geology*, v. 67, p. 551-578.

786 Ohmoto, H. and Rye, R.O., 1979, Isotopes of sulfur and carbon. In: Barnes, H.I. (Editor),  
787 Geochemistry of hydrothermal ore deposits. 2nd Edition, John Wiley and Sons, New York,  
788 pp. 509-567.

789 Papineau, D., De Gregorio, B. T., Cody, G. D., Fries, M. D., Mojzsis, S. J., Steele, A., Stroud, R. M. and  
790 Fogel, M. L., 2010, Ancient graphite in the Eoarchean quartz–pyroxene rocks from Akilia in  
791 southern West Greenland I: Petrographic and spectroscopic characterization: *Geochimica et  
792 Cosmochimica Acta*, v. 74, p. 5862-5883.

793 Parra-Avila, L. A., Belousova, E., Fiorentini, M. L., Baratoux, L., Davis, J., Miller, J. and Mccuaig, T. C.,  
794 2016, Crustal evolution of the Paleoproterozoic Birimian terranes of the Baoulé-Mossi  
795 domain, southern West African Craton: U–Pb and Hf-isotope studies of detrital zircons:  
796 *Precambrian Research*, v. 274, p. 25-60.

797 Parra-Avila, L. A., Belousova, E., Fiorentini, M. L., Eglinger, A., Block, S. and Miller, J., 2018, Zircon Hf  
798 and O-isotope constraints on the evolution of the Paleoproterozoic Baoulé-Mossi domain of  
799 the southern West African Craton: *Precambrian Research*, v. 306, p. 174-188.

800 Parra-Avila, L. A., Bourassa, Y., Miller, J., Perrouty, S., Fiorentini, M. L. and Campbell Mccuaig, T.,  
801 2015, Age constraints of the Wassa and Benso mesothermal gold deposits, Ashanti Belt,  
802 Ghana, West Africa: *Journal of African Earth Sciences*, v. 112, p. 524-535.

803 Pass, H. E., Cooke, D. R., Davidson, G., Maas, R., Dipple, G., Rees, C., Ferreira, L., Taylor, C. and Deyell,  
804 C. L., 2014, Isotope geochemistry of the Northeast zone, Mount Polley alkalic Cu-Au-Ag  
805 porphyry deposit, British Columbia: A case for carbonate assimilation: *Economic Geology*, v.  
806 109, p. 859-890.

807 Perrouty, S., Aillères, L., Jessell, M. W., Baratoux, L., Bourassa, Y. and Crawford, B., 2012, Revised  
808 Eburnean geodynamic evolution of the gold-rich southern Ashanti Belt, Ghana, with new  
809 field and geophysical evidence of pre-Tarkwaian deformations: *Precambrian Research*, v.  
810 204, p. 12-39.

811 Petersson, A., Scherstén, A. and Gerdes, A., 2018, Extensive reworking of Archaean crust within the  
812 Birimian terrane in Ghana as revealed by combined zircon U-Pb and Lu-Hf isotopes:  
813 *Geoscience Frontiers*, v. 9, p. 173-189.

814 Phillips, G. N. and Powell, R., 1993, Link between gold provinces: *Economic Geology*, v. 88, p. 1084-  
815 1098.

816 Phillips, G. N. and Powell, R., 2010, Formation of gold deposits: a metamorphic devolatilization  
817 model: *Journal of Metamorphic Geology*, v. 28, p. 689-718.

818 Pitcairn, I. K., Teagle, D. A., Craw, D., Olivo, G. R., Kerrich, R., and Brewer, T. S., 2006, Sources of  
819 metals and fluids in orogenic gold deposits: insights from the Otago and Alpine Schists, New  
820 Zealand: *Economic Geology*, v. 101, p. 1525-1546.

821 Pitcairn, I. K., Craw, D., and Teagle, D. A., 2014, The gold conveyor belt: Large-scale gold mobility in  
822 an active orogen: *Ore Geology Reviews*, v. 62, p. 129-142.

823 Riehl, W. and Cabral, A.R., 2018, Meta-evaporite in the Carajás mineral province, northern Brazil:  
824 *Mineralium Deposita*, v. 53, p. 895-902.

825 Robinson, B. W. and Kusakabe, M., 1975, Quantitative preparation of sulfur dioxide, for sulfur-  
826 34/sulfur-32 analyses, from sulfides by combustion with cuprous oxide: *Analytical Chemistry*,  
827 v. 47, p. 1179-1181.

828 Randgold Resources Ltd., 2017, Annual report. [www.randgoldresources.com](http://www.randgoldresources.com)

829 Rosenbaum, J. and Sheppard, S. M. F. 1986, An isotopic study of siderites, dolomites and ankerites at  
830 high temperatures: *Geochimica et Cosmochimica Acta*, v. 50, p. 1147-1150.

831 Rye, R. O. and Ohmoto, H., 1974, Sulfur and carbon isotopes and ore genesis: a review: *Economic*  
832 *Geology*, v. 69, p. 826-842.

833 Samperton, K. M., Bell, E. A., Barboni, M., Keller, C. B. and Schoene, B., 2017, Zircon age-  
834 temperature-compositional spectra in plutonic rocks: *Geology*, v. 45, p. 983-986.

835 Schidlowski, M., Eichmann, R. and Junge, C. E., 1975, Precambrian sedimentary carbonates: carbon  
836 and oxygen isotope geochemistry and implications for the terrestrial oxygen budget:  
837 *Precambrian Research*, v. 2, p. 1-69.

838 Schwartz, M. and Melcher, F., 2004, The Faleme Iron District, Senegal. *Economic Geology*, v. 99, p.  
839 917-939.

840 Schwinn, G., Wagner, T., Baatartsogt, B. and Markl, G., 2006, Quantification of mixing processes in  
841 ore-forming hydrothermal systems by combination of stable isotope and fluid inclusion  
842 analyses: *Geochimica et Cosmochimica Acta*, v. 70, p. 965-982.

843 Sharp, Z., 2017, Principles of stable isotope geochemistry ([digitalrepository.unm.edu](http://digitalrepository.unm.edu)).

844 Shelton, K. L., 1983, Composition and origin of ore-forming fluids in a carbonate-hosted porphyry  
845 copper and skarn deposit; a fluid inclusion and stable isotope study of Mines Gaspé, Quebec:  
846 *Economic Geology*, v. 78, p. 387-421.

847 Sheppard, S. M. F., 1986, Chapter 6. Characterization and Isotopic Variations in Natural Waters:  
848 *Stable Isotopes in High Temperature Geological Processes*.

849 Spence-Jones, C. P., Jenkin, G. R. T., Boyce, A. J., Hill, N. J. and Sangster, C. J. S., 2018, Tellurium,  
850 magmatic fluids and orogenic gold: An early magmatic fluid pulse at Cononish gold deposit,  
851 Scotland: *Ore Geology Reviews*, v. 102, p. 894-905.

852 Strauss, H. and Moore, T., 1992, Abundances and isotopic compositions of carbon and sulfur species  
853 in whole rock and kerogen samples: *The Proterozoic biosphere: A multidisciplinary study*, pp.  
854 709-798.

855 Taylor, H., 1974, The application of oxygen and hydrogen isotope studies to problems of  
856 hydrothermal alteration and ore deposition: *Economic geology*, v. 69, p. 843-883.

857 Taylor, P. N., Moorbath, S., Leube, A. and Hirdes, W., 1992, Early Proterozoic crustal evolution in the  
858 Birimian of Ghana: constraints from geochronology and isotope geochemistry: *Precambrian*  
859 *Research*, v. 56, p. 97-111.

- 860 Thébaud, N., Allibone, A., Masurel, Q., Eglinger, A., Davis, J., André-Mayer, A., Miller, J. And Jessell,  
861 M, The Paleoproterozoic (Rhyacian) gold deposits of West Africa: *Society of Economic*  
862 *Geologists Special Publication 23*, 2020, in press.
- 863 Tomkins, A. G., 2013, On the source of orogenic gold. *Geology*, v. 41, p. 1255-1256.
- 864 Trail, D., Bindeman, I. N., Watson, E. B. and Schmitt, A. K., 2009, Experimental calibration of oxygen  
865 isotope fractionation between quartz and zircon: *Geochimica et Cosmochimica Acta*, v. 73, p.  
866 7110-7126.
- 867 Treloar, P., Lawrence, D., Senghor, D., Boyce, A. and Harbidge, P., 2015, The Massawa gold deposit,  
868 Eastern Senegal, West Africa: an orogenic gold deposit sourced from magmatically derived  
869 fluids? *Geological Society, London, Special Publications*, v. 393, p. 135-160.
- 870 Tshibubudze, A., Hein, K. A. and Mccuaig, T. C., 2015, The relative and absolute chronology of strato-  
871 tectonic events in the Gorom-Gorom granitoid terrane and Oudalan-Gorouol belt, northeast  
872 Burkina Faso: *Journal of African Earth Sciences*, v. 112, p. 382-418.
- 873 Valley, J. W., 1986, Stable isotope geochemistry of metamorphic rocks: *Reviews in Mineralogy and*  
874 *Geochemistry*, v. 16, p. 445-489.
- 875 Van Hinsberg, V. J., Henry, D. J. and Marschall, H. R., 2011, Tourmaline: an ideal indicator of its host  
876 environment: *The Canadian Mineralogist*, v. 49, p. 1-16.
- 877 Vidal, M., Gumiaux, C., Cagnard, F., Pouclet, A., Ouattara, G. and Pichon, M., 2009, Evolution of a  
878 Paleoproterozoic “weak type” orogeny in the West African Craton (Ivory Coast):  
879 *Tectonophysics*, v. 477, p. 145-159.
- 880 White, A., Burgess, R., Charnley, N., Selby, D., Whitehouse, M., Robb, L. and Waters, D., 2014,  
881 Constraints on the timing of late-Eburnean metamorphism, gold mineralisation and regional  
882 exhumation at Damang mine, Ghana: *Precambrian Research*, v. 243, p. 18-38.
- 883 Williams, P. J., Barton, M. D., Johnson, D. A., Fontboté, L., De Haller, A., Mark, G., Oliver, N. H. and  
884 Marschik, R., 2005, Iron oxide copper-gold deposits: Geology, space-time distribution, and  
885 possible modes of origin: *Economic Geology*, pp. 371-405.
- 886 Wyman, D. A., Cassidy, K. F. and Hollings, P., 2016, Orogenic gold and the mineral systems approach:  
887 Resolving fact, fiction and fantasy: *Ore Geology Reviews*, v. 78, 322-335.
- 888 Xavier, R. P., Wiedenbeck, M., Trumbull, R. B., Dreher, A. M., Monteiro, L. V., Rhede, D., De Araújo, C.  
889 E. and Torresi, I., 2008, Tourmaline B-isotopes fingerprint marine evaporites as the source of  
890 high-salinity ore fluids in iron oxide copper-gold deposits, Carajas Mineral Province (Brazil) :  
891 *Geology*, v. 36, p. 743-746.
- 892 Xue, Y., Campbell, I., Ireland, T. R., Holden, P. and Armstrong, R., 2013, No mass-independent sulfur  
893 isotope fractionation in auriferous fluids supports a magmatic origin for Archean gold  
894 deposits: *Geology*, v. 41, p. 791-794.
- 895 Yardley, B. W. and Cleverley, J. S., 2015, The role of metamorphic fluids in the formation of ore  
896 deposits: *Geological Society, London, Special Publications*, v. 393, p. 117-134.
- 897 Zheng, Y.-F., 1993, Calculation of oxygen isotope fractionation in hydroxyl-bearing silicates: *Earth*  
898 *and Planetary Science Letters*, v. 120, p. 247-263.
- 899 Zheng, Y.-F., 1999, Oxygen isotope fractionation in carbonate and sulfate minerals: *Geochemical*  
900 *Journal*, v. 33, p. 109-126.

901

902

903 **Table captions**

904 Table 1 – Summary of key characteristics of Au and Fe mineralization in the Loulo District.

905 Table 2 - Table summarising stable sulfur isotope data from the Loulo Mining District. \* - denotes data  
906 from Fouillac et al. (1993). † - denotes data from Lawrence et al. (2013b). ‡ - denotes data from  
907 Lambert-Smith et al. (2016b).

908 Table 3 – Table summarising stable carbon and oxygen isotope data from the Loulo Mining District. \*  
909 - denotes data from Fouillac et al. (1993). † - denotes data from Lawrence et al. (2013b). ‡ - denotes  
910 data from Lambert-Smith et al. (2016b).

911 Table 4 – Chemical and isotopic fluid compositions used for end member components in fluid mixing  
912 and fluid-rock reaction models.

913 **Figure captions**

914 Fig. 1. Geological map of the southern West Africa Craton, highlighting the distribution of Au deposits  
915 (Modified after Baratoux et al., 2011; Fontaine et al., 2017; Thebaud et al. In Press). Location of major  
916 Au deposits are based on those reported in Markwitz et al. (2016), and Goldfarb et al. (2017).

917 Fig. 2. Geological map of the Loulo Mining District in the south eastern region of the Kédougou-  
918 Kéniéba inlier, with studied Au occurrences highlighted. Modified after Lawrence et al. (2013a), and  
919 Lambert-Smith et al. (2016c).

920 Fig. 3. Key alteration and ore mineral textures at Karakaene Ndi. (A) photograph of coarse epidote-  
921 albite-calcite vein cross cutting albitized igneous rock with envelopes of dark green actinolite  
922 replacement in the wall rock and Fe-rich halos encroaching on the albitized rock. Photomicrographs of  
923 (B) albitized wall rock with relict phenocrysts (replaced by albite) (XPL); (C) fine fibrous actinolite  
924 replacing wall rock with minor magnetite mineralization (PPL); (D) albitized wall rock overprinted by  
925 Fe-rich carbonate and disseminated actinolite with minor pyrite (PPL) and; (E) coarse intergrown  
926 epidote and albite in cross cutting vein (XPL). Photographs of ore textures in diamond drill core from  
927 Karakaene Ndi showing: (F) massive magnetite replacement with weak disseminated pyrite overprint  
928 and; (G) late calcite-pyrite-chlorite vein cross cutting magnetite mineralization.

929 Fig. 4. Field photographs showing (A) typical marly dolostones country rock with highly deformed  
930 calcite veining, argillaceous layers and graphitic material. (B) Ankerite-quartz-pyrite stockwork ore  
931 characteristic of the Gara and Goukoto deposit (highly subordinate in the latter), the P64 satellite, and  
932 the Baqata and Kolya exploration targets. (C) Auriferous ankerite-quartz-pyrite veins cross cutting  
933 phyllic wall rock alteration at the Yalea deposit. (D) An example of sulfide-bearing carbonate veins  
934 with Au concentrations below the detection limit of fire assay in the meter of core sampled. (E) Barren

935 veining in unaltered and unmineralized Kofi Series metasedimentary country rock. (F) Folded, sulfide-  
936 free veining in weakly altered, unmineralized metasedimentary host rock. (G) Sulfide-bearing veins  
937 from the Kofi Series with fire assay results below detection limit (<0.01 ppm).

938 Fig. 5. Histograms showing  $\delta^{34}\text{S}$  data from pyrite at (A) the Loulo Au deposits (Fouillac et al., 1993,  
939 Lawrence et al., 2013b, Lambert-Smith et al., 2016b, Lambert-Smith, 2014b) and diagenetic pyrite from  
940 the Kofi series dolostones, (B) the Kabe West, Kolya, Baqata and Bobotie exploration targets, (C) the  
941 Karakaene Ndi skarn deposit, with paragenetic breakdown between sulfides disseminated in the iron ore  
942 and those hosted in cross cutting veins (inset).

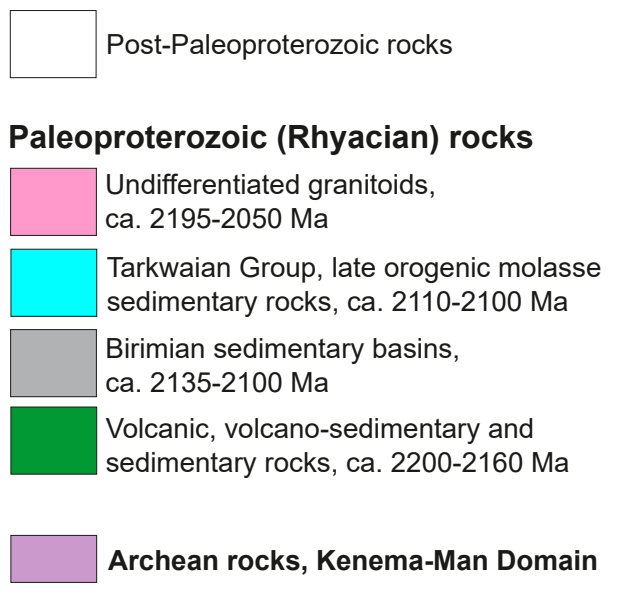
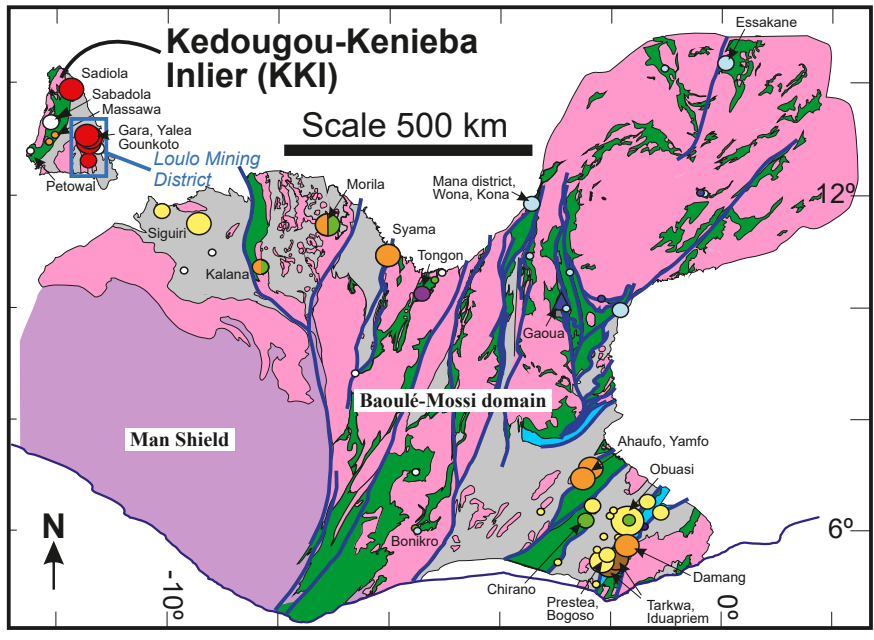
943 Fig. 6. Histograms showing  $\delta^{13}\text{C}$  data from (A) ankerite and dolomite in auriferous hydrothermal veins,  
944 barren hydrothermal veins, and carbonate country rocks from the Loulo-Goukoto complex, including  
945 the Gara, Yalea and Goukoto mines (data from Fouillac et al., 1993, Lawrence et al., 2013b, Lambert-  
946 Smith et al., 2016b); (B) ankerite and dolomite in auriferous and barren hydrothermal veins from the  
947 Bambadji exploration targets, Gefa, Boboti, Kabe West, Kolya and Baqata; (C) calcite from late  
948 hydrothermal veins at the Karakaene Ndi iron skarn deposit. Fields of typical C-isotope characteristics  
949 of Precambrian marine carbonates and organic carbon are indicated (Schidlowski et al., 1975, Eichmann  
950 and Schidlowski, 1975). Histograms showing  $\delta^{18}\text{O}$  data from (D) ankerite and dolomite in auriferous  
951 hydrothermal veins, barren hydrothermal veins, and carbonate country rocks from the Loulo-Goukoto  
952 complex; (E) ankerite and dolomite in auriferous and barren hydrothermal veins from the Bambadji  
953 exploration targets, Gefa, Boboti, Kabe West, Kolya and Baqata; (F) calcite from late hydrothermal  
954 veins at the Karakaene Ndi iron skarn deposit. Number of samples and key is equivalent to (A), (B) and  
955 (C).

956 Fig. 7.  $\delta^{18}\text{O}$  versus  $\delta^{13}\text{C}$  plot showing isotopic compositions of ore related carbonate at Au deposits and  
957 exploration targets in the Loulo District, in addition to compositional ranges of Kofi Series dolostones  
958 and barren carbonate veining. Black curve with open circles represents C-O isotopic compositions  
959 expected in carbonates precipitated from a mixture of aqueous-carbonic fluid with a starting  
960 composition of  $\delta^{18}\text{O} = 10.2 \text{ ‰}$  and  $\delta^{13}\text{C} = -27 \text{ ‰}$  and a magmatic fluid with a starting composition of  
961  $\delta^{18}\text{O} = 9.4 \text{ ‰}$  and  $\delta^{13}\text{C} = -6 \text{ ‰}$  (red star). Black curve with grey circles represents C-O isotopic values  
962 expected in carbonates precipitated from a mixture of the same aqueous-carbonic fluid with a brine of  
963 meta-evaporite origin and starting isotopic composition of  $\delta^{18}\text{O} = 16.2 \text{ ‰}$  and  $\delta^{13}\text{C} = -2.6 \text{ ‰}$  (blue star).  
964 Red curve represents C-O isotopic fluid values resulting from the magmatic fluid reacting with the Kofi  
965 Series dolostones (light grey field; average composition of  $\delta^{18}\text{O} = 21 \text{ ‰}$  and  $\delta^{13}\text{C} = -0.5 \text{ ‰}$ ). The curve  
966 was modelled at  $550 \text{ °C}$   $\text{XCO}_2$  of 0.11. Blue, violet, and purple curves represent isotopic compositions  
967 resulting from reaction between the aqueous-carbonic fluid and the Kofi dolostones at 295, 325, and  
968  $400 \text{ °C}$ , respectively and at  $\text{XCO}_2$  of 0.2. Isotopic compositional ranges for magmatic fluids (red field)



969 (Ohmoto, 1972) and Precambrian marine carbonates (blue field) (Eichmann and Schidlowski, 1975) are  
970 given for reference.

971 Fig. 8. Cartoon cross section showing (A) Kofi Series metasedimentary rocks, including evaporite  
972 bearing dolostone horizons in the west of the Series, these are folded and metamorphosed prior to 2085  
973 Ma, with minor albitisation indicating the presence of early saline brines. (B) Intrusion of the Falémé  
974 Batholith from approx. 2085 Ma increases the local geothermal gradient and exsolves magmatic-  
975 hydrothermal fluid. This event may both promote devolatilization of the dolostones in the Western Kofi  
976 Series and allow water-rock reaction between the magmatic fluids and the evaporite-bearing marly  
977 dolostones; this gives rise to a hybridized hypersaline magmatic-evaporitic brine, which circulates  
978 through the metasedimentary rocks leading to the development of albitized and tourmalinized rock  
979 packages. (C) Between 2085 and 2070 Ma hybrid brines continue to circulate, aqueous-carbonic fluids  
980 are introduced along significant structures in the Kofi Series and further magmatism in the Falémé  
981 batholith leads to emplacement of small stocks and dikes which extend into the Kofi Series. The  
982 aqueous-carbonic fluid unmixes in response to pressure fluctuations, contributing to Au mineralization;  
983 at Gara and several other deposits this process is enhanced by partial mixing with hybrid hypersaline  
984 brines. Minor amounts of magmatic-hydrothermal fluid derived from dikes cross cutting the Kofi Series  
985 may contribute volatiles directly to some of the minor mineralized rock packages in the west of the  
986 Loulo Au system. Magnetite skarn deposits simultaneously develop within and adjacent to small dioritic  
987 stocks in the Falémé batholith and western Kofi Series.



**Gold deposit styles**

- Post-collision, orogenic
- Tarkwaian paleoplacer
- skarn
- Post-collision, Loulo/Falémé
- Eburnean basin orogenic
- Eoeburnean orogenic
- Granitoid-hosted
- Eburnean orogenic, part or wholly hosted by Eoeburnian rocks

**Gold deposit size**

- > 50 Moz
- 8 - 50 Moz
- 3 - 8 Moz
- < 3 Moz





5 km

UTM 29N




N

# Legend


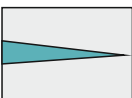
## Post-Birimian lithologies

-  Dolerite
-  Intense albitisation
-  Strong albitisation (protolith identifiable)
-  Iron skarn mineralisation


## Altered rocks

-  Faleme batholith plutonic rocks
-  Volcaniclastic and sedimentary rocks
-  Rhyolitic breccia

## Igneous lithologies

-  Marly and variably altered marble
-  Sandstones, siltstones, wackes and argillites with polymict conglomerate

 Bedding

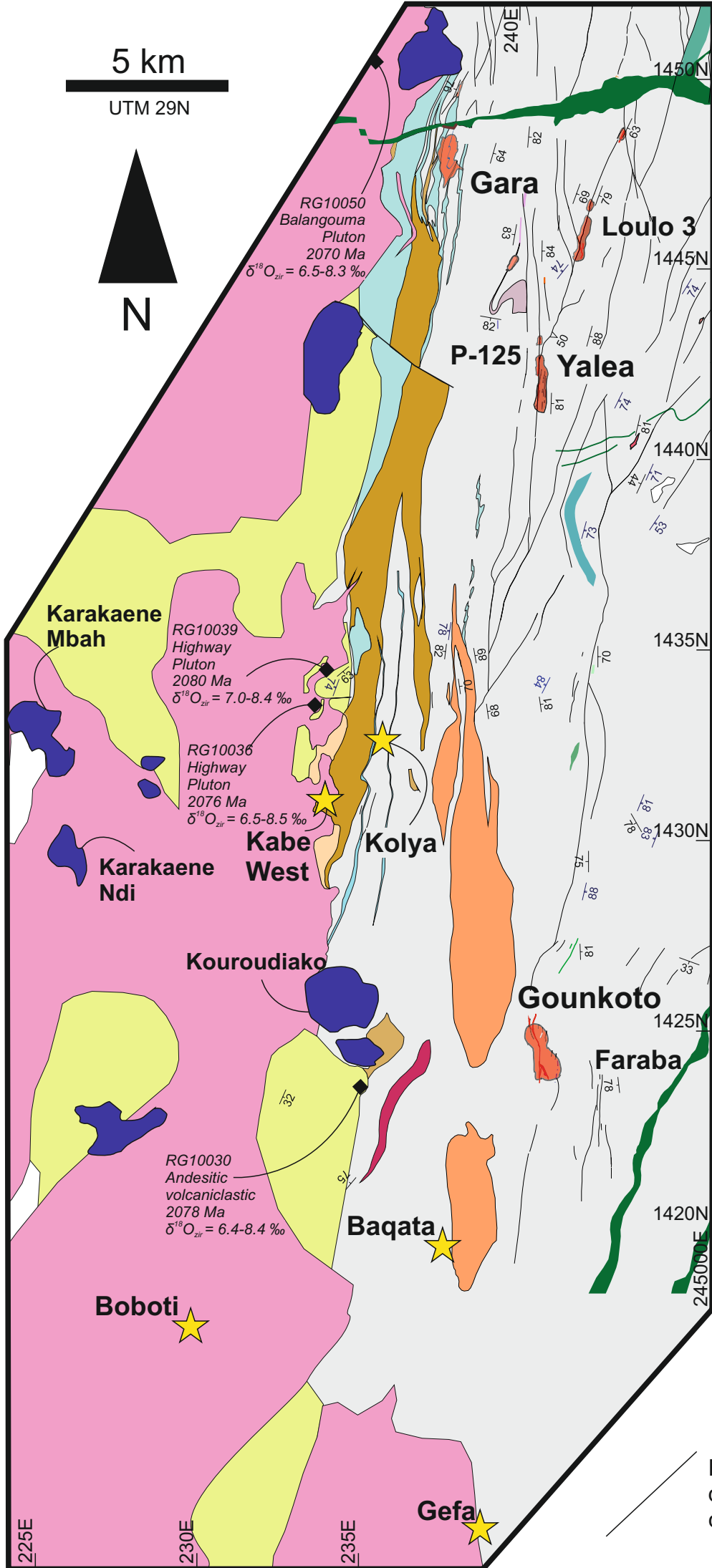
 S<sub>2L</sub> cleavage

 Magmatic and volcanic rock samples with  $\delta^{18}O_{zircon}$  data

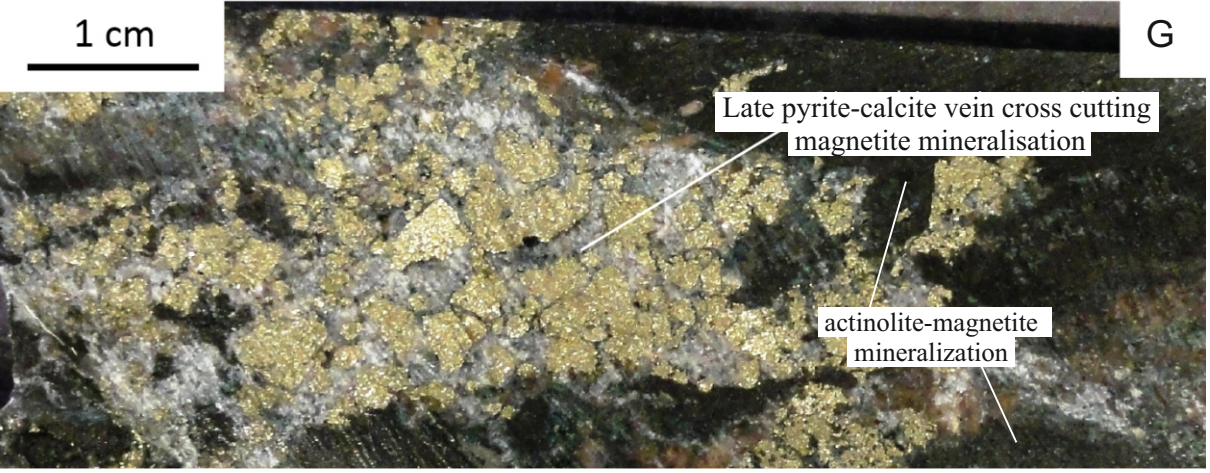
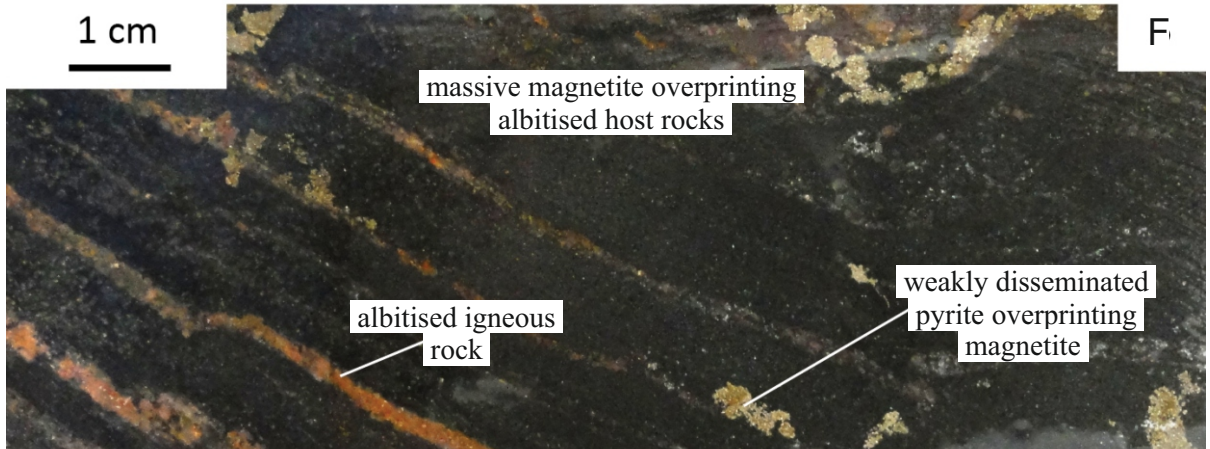
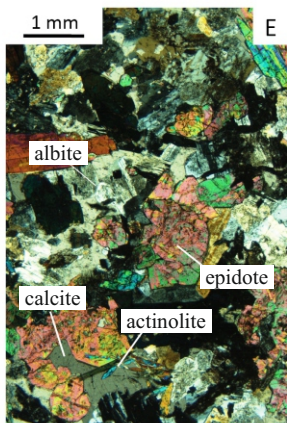
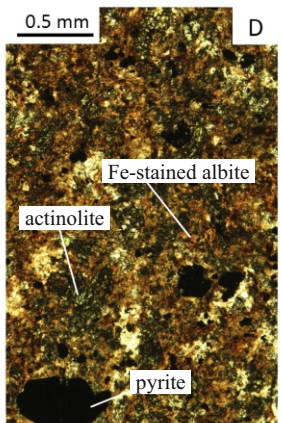
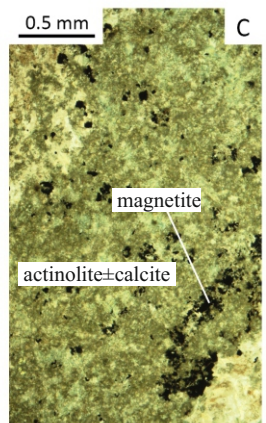
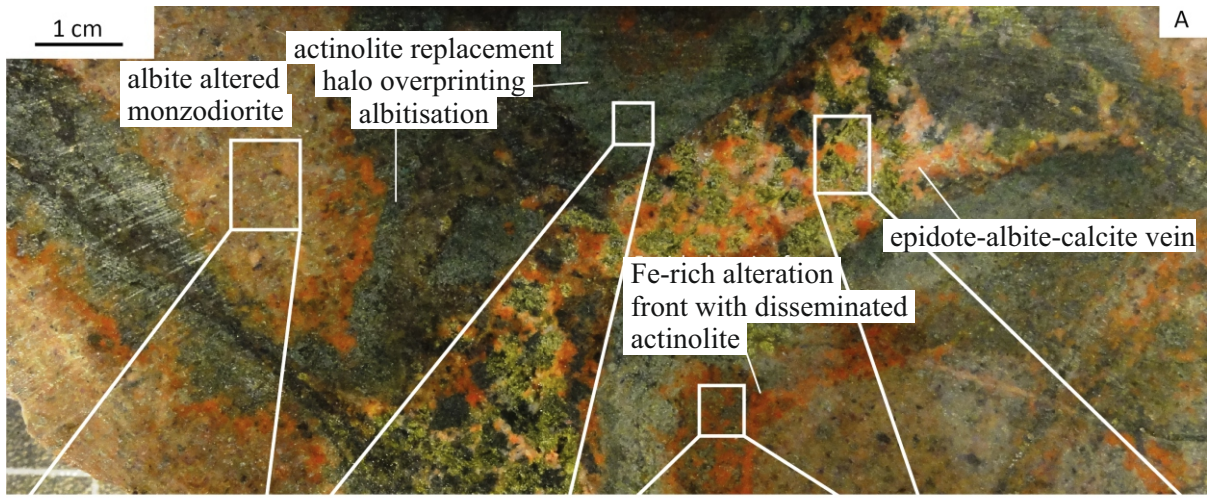
 Exploration targets

 Au mine

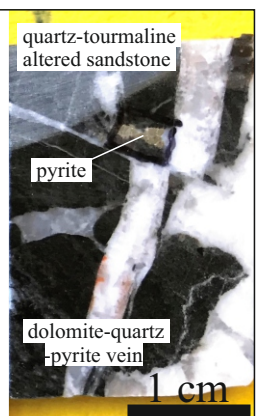
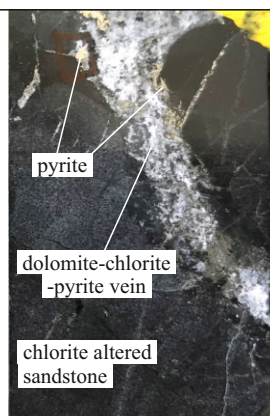
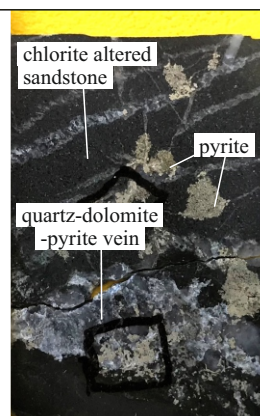
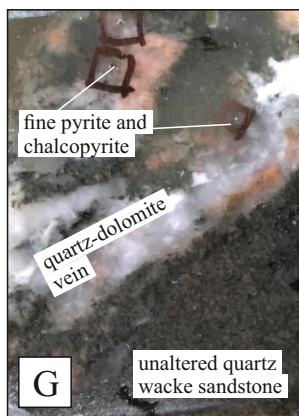
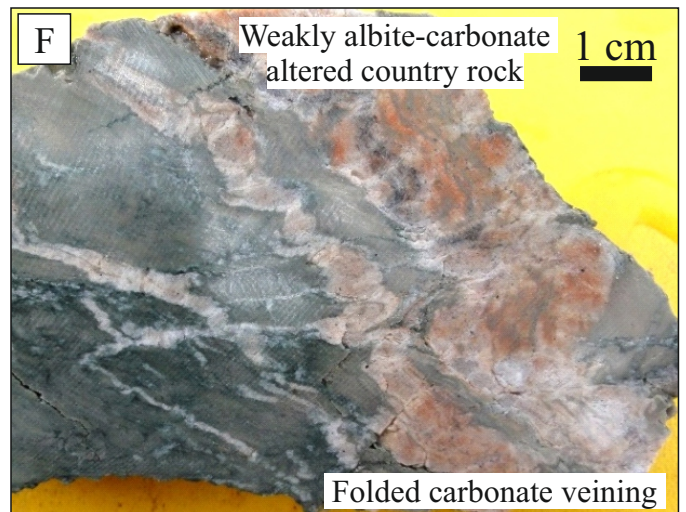
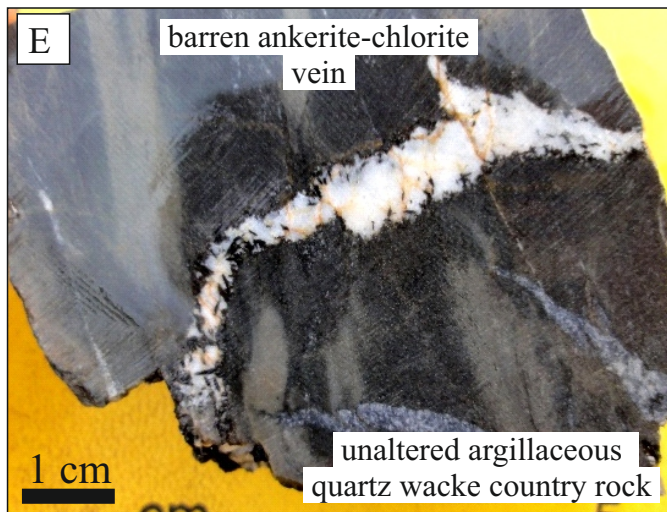
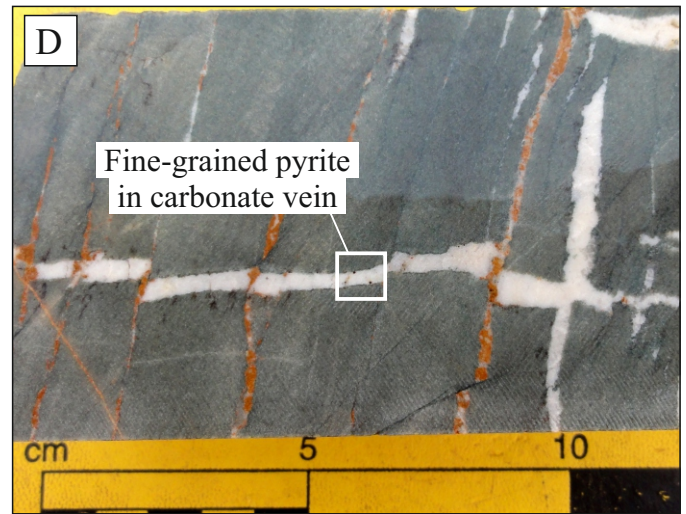
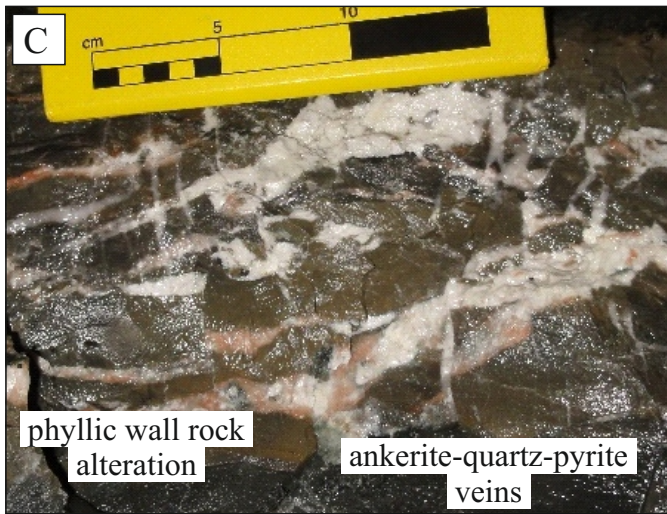
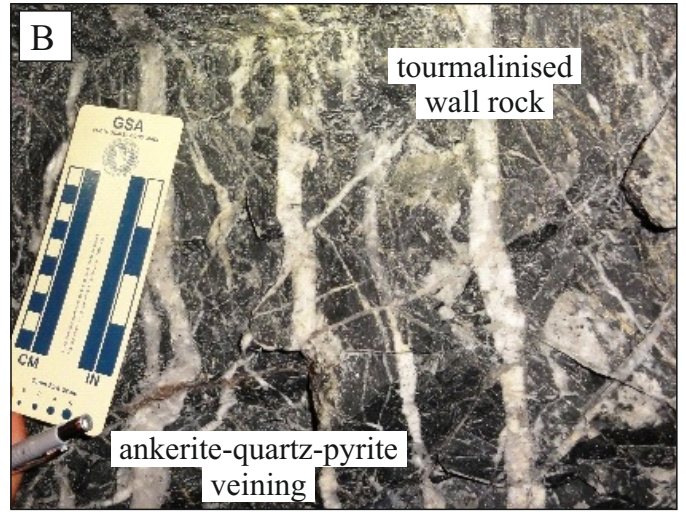
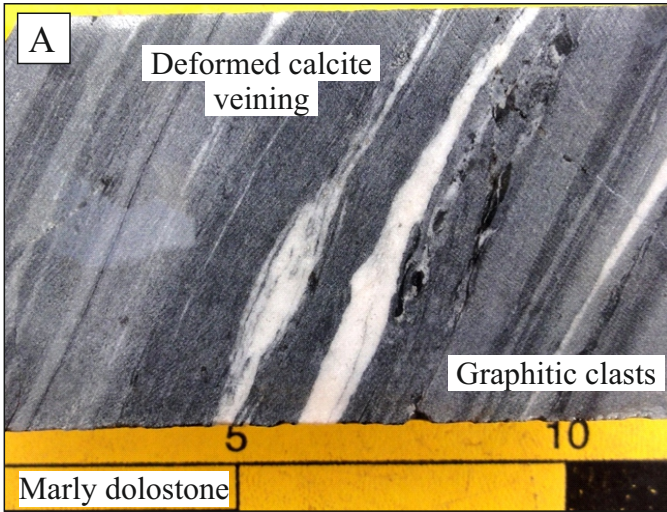
Faults, fractures and shear zones from drilling and outcrop and inferred from chargeability and VTEM data



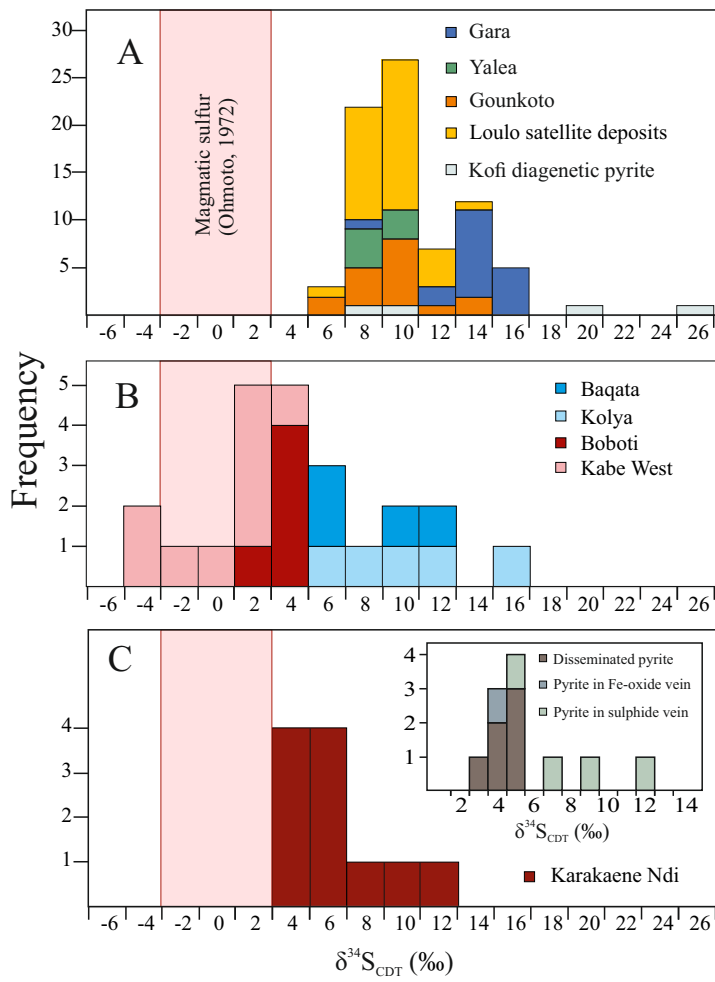


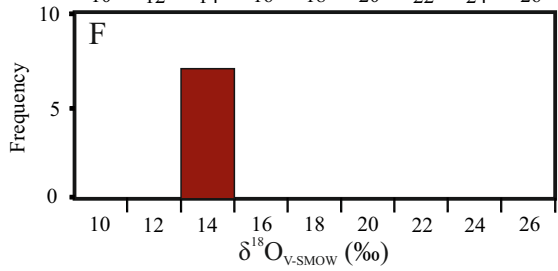
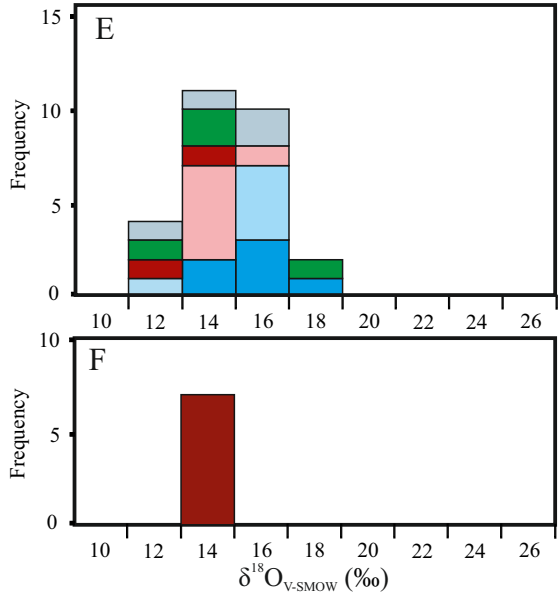
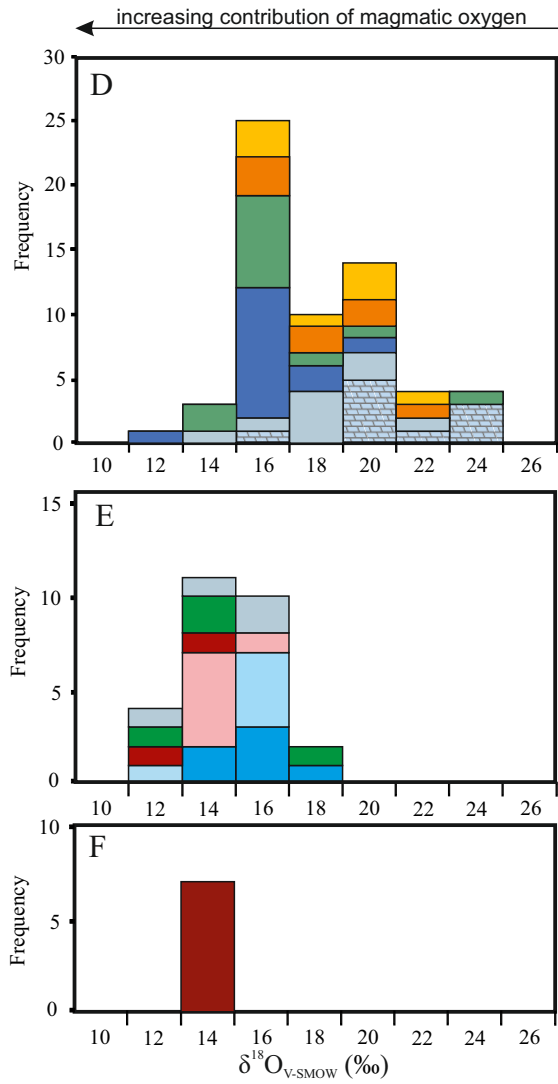
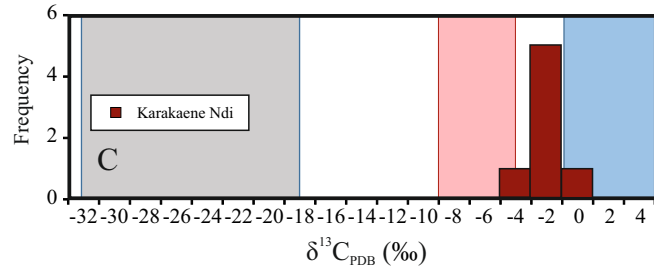
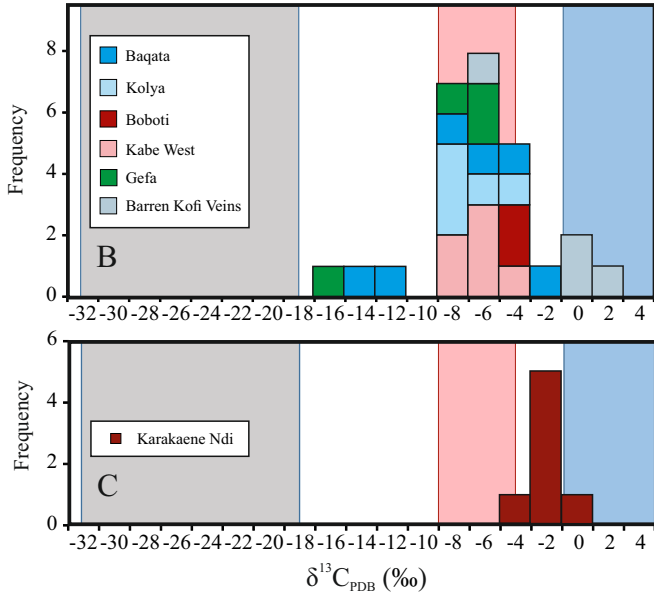
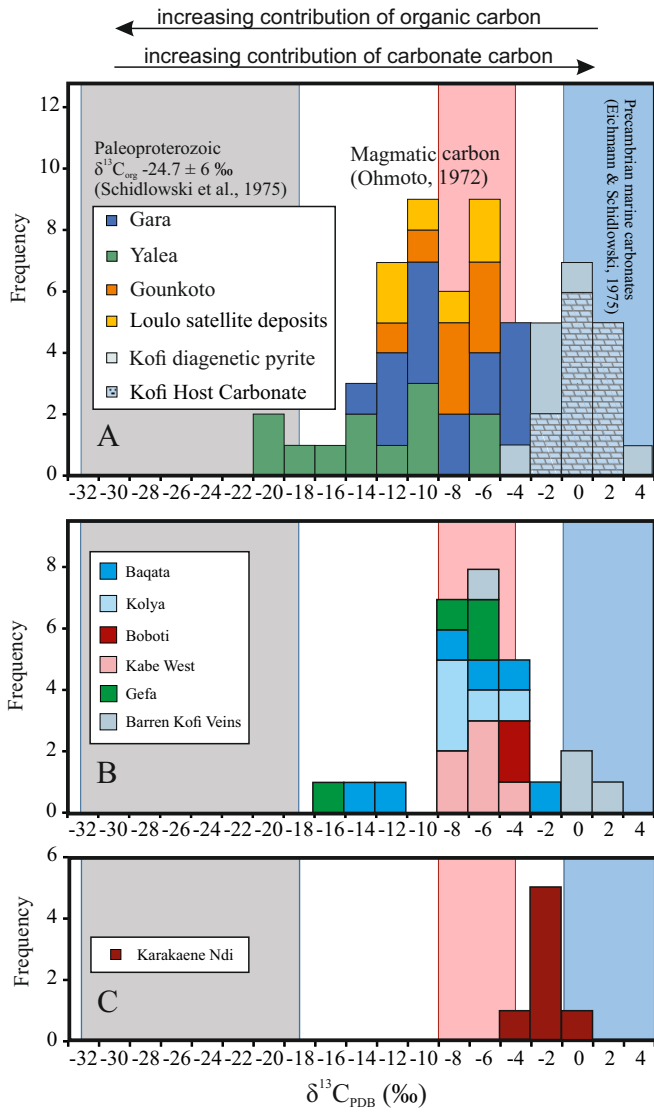


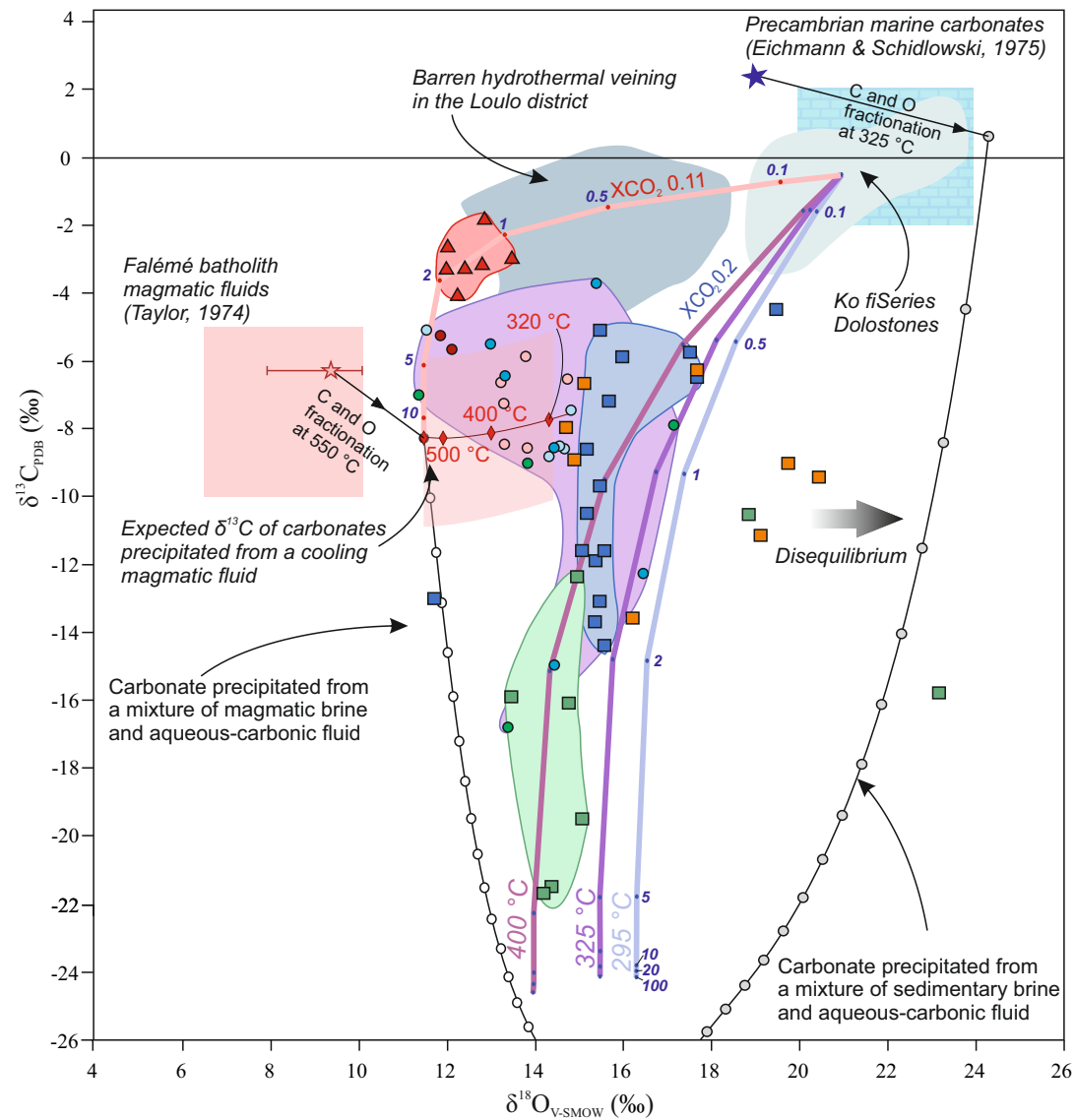












### Legend

**Deposits >3 Moz**

- Gara
- Yalea
- Goukoto

**Exploration targets**

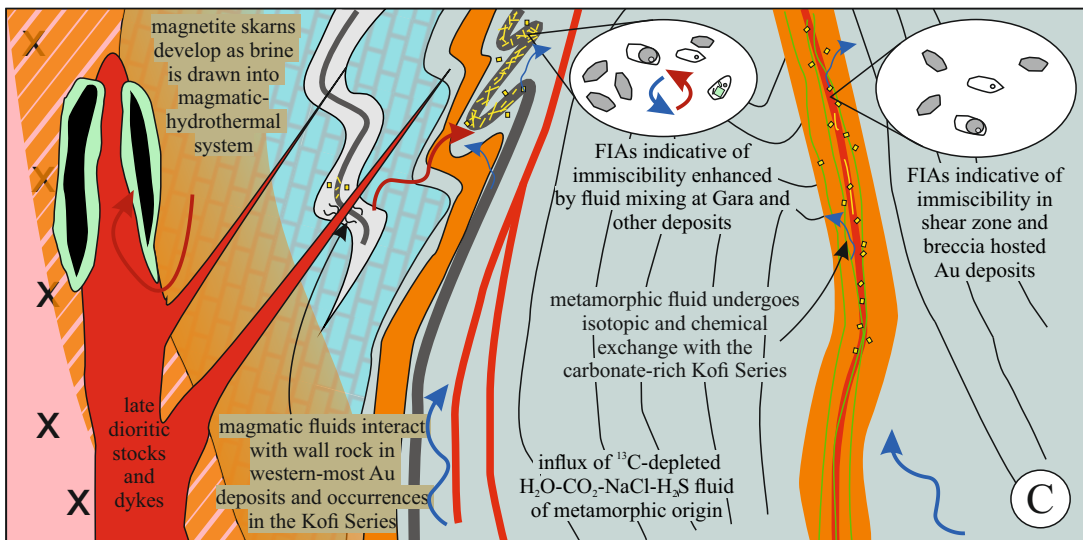
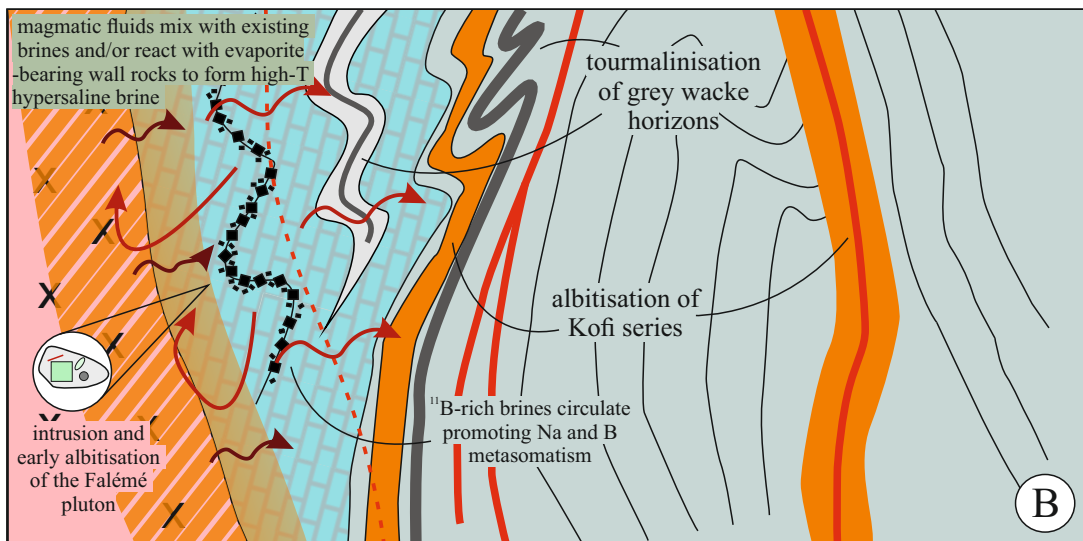
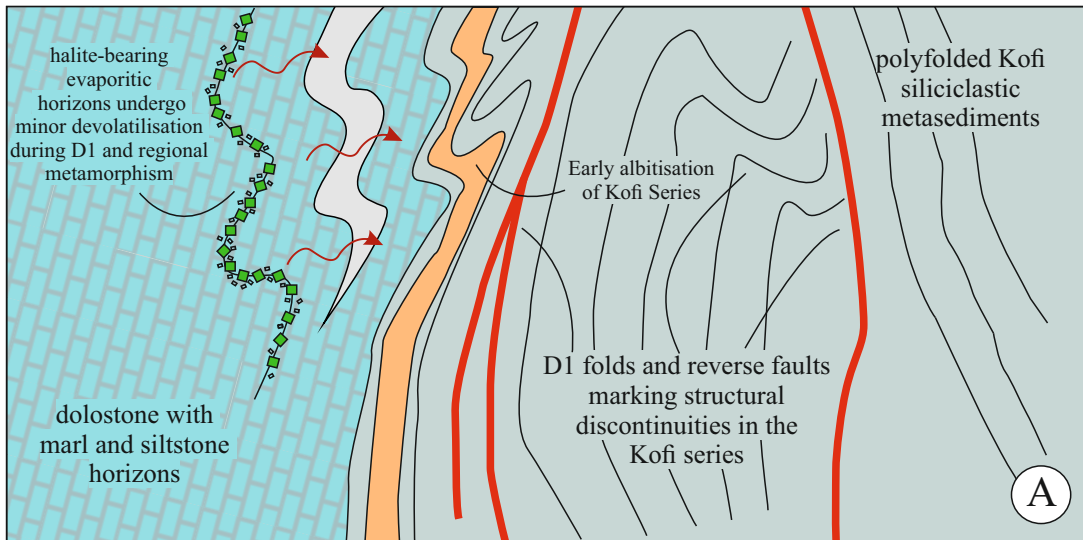
- Boboti
- Kolya
- Baqata
- Kabe West
- Gefa

**Other features:**

- Karakaene Ndi Fe skarn
- Barren veins
- Kofi dolostones
- Magmatic fluid range
- Falémé magmatic fluid
- Isotopic composition of sedimentary brine

**Au mineralization**





Ore Body	Key ore textures	Ore mineralogy	Alteration styles	P-T conditions	Constraint	Reference
<b>Gold</b>						
<b>Gara</b>	carbonate-quartz-pyrite vein stockwork	pyrite ( $\pm$ Ni-Co)-monazite-xenotime-scheelite-gold-chalcopyrite-gersdorffite-pentlandite-Ni-pyrrhotite-arsenopyrite-molybdenite	Tourmalinisation and minor albitisation	>340 °C at 1.75 kbar	Fluid inclusions, O-isotope equilibria, arsenopyrite geothermometry	Lawrence et al. (2013a, b)
<b>Yalea</b>	Shear zone hosted sulphide stringers and hydrothermal breccia	arsenian pyrite-arsenopyrite-chalcopyrite-gold-pyrrhotite-jamesonite-galena-scheelite-tennantite	Early albitisation and syn-mineralisation chloritisation	320 °C at 1.45 Kbar (5.4 km)	Fluid inclusions, arsenopyrite and chlorite geothermometry, O-isotope equilibria	Lawrence et al. (2013a, b)
<b>Goukoto</b>	Shear zone hosted sulphide stringers and hydrothermal breccia	pyrite ( $\pm$ As)-arsenopyrite-pyrrhotite-chalcopyrite-magnetite-haematite-gold-monzazite-scheelite-gersdorffite-cobaltite-tennantite-altaite-tellurium-callaverite-sylvanite-petzite	Early albitisation and syn-mineralisation chloritisation - minor tourmalinisation	340 °C at 1.4 Kbar (5.2 km)	Fluid inclusions, arsenopyrite and chlorite geothermometry, O-isotope equilibria	Lambert-Smith et al. (2016b)
<b>Faraba</b>	Quartz-dolomite veining, sulfide-chlorite-magnetite veining and disseminated	arsenian pyrite - arsenopyrite - magnetite-pyrrhotite - chalcopyrite - gold - tsumoite - altaite - hedleyite - bismuth	Early albitisation and syn-mineralisation chloritisation	-		
<b>Sub-economic gold</b>						
<b>Baqata</b>	carbonate-quartz-pyrite vein stockwork and disseminated	pyrite ( $\pm$ Ni-As) - chalcopyrite-pyrrhotite-monazite-scheelite-xenotime-gold-millerite-polydymite-sternbergite-tellurobismuthite-calaverite-bismuth	Tourmalinisation and albitisation	$\sim$ 315 °C at 1.3 Kbar (4.8 km)	Fluid inclusions, chlorite geothermometry	Lambert-Smith (2014)
<b>Kolya</b>	carbonate-quartz-pyrite vein stockwork	pyrite - chalcopyrite-arsenian pyrite- scheelite-monazite-xenotime-gold-tellurobismuthite-altaite-melonite	Tourmalinisation and minor actinolite replacement	>300 °C	Fluid inclusions (minimum trapping)	Lambert-Smith (2014)
<b>Kabe West</b>	Hydrothermal breccia - carbonate vein stockwork	pyrite ( $\pm$ Ni-Co) - chalcopyrite-monazite-gold-xenotime-altaite-melonite	Albitisation + weak tourmaline	$\sim$ 308 °C	O-isotope equilibria	Lambert-Smith (2014)
<b>Boboti</b>	Hydrothermal veining	pyrite - monazite-gold-haematite-titanite	Weak albitisation	-		
<b>Gefa</b>	carbonate-quartz-pyrite vein stockwork and weakly disseminated	pyrite - chalcopyrite	Tourmalinisation and albitisation	-		
<b>Iron</b>						
<b>Karakaene Ndi</b>	Massive magnetite with late disseminated and vein hosted sulphides	magnetite - haematite - pyrite (N i $\pm$ As substitution)-apatite-chalcopyrite-monazite-gold-uraninite-bismuth-clausenthalite	Early albitisation overprinted by calc-silicate and magnetite replacement	500 °C at 2.5 kbar	Fluid inclusions, O-isotope equilibria	Lambert-Smith (2014)

<b>Deposit / Target</b>	<b>Sample</b>	<b><math>\delta^{34}\text{S}</math>(‰ vs. CDT)</b>	<b>Mineral</b>	<b>Notes</b>	
<b>Host Rock</b>					
Diagenetic pyrite in dolostone	JLSB09	19.70	Pyrite		
	JLSB07	25.10	Pyrite		
	07YD52	9.00	pyrite		
	07YD89	6.40	pyrite		
<b>Target</b>					
Kolya	JLSB08	9.30	Pyrite		
	JLSB29	14.20	Pyrite		
	JLSB30	7.00	Pyrite		
	JLSB31	4.20	Pyrite		
	JLSB06	10.20	Pyrite		
Boboti	JLSB15	2.60	Pyrite		
	JLSB16	2.20	Pyrite		
	JLSB17	3.90	Pyrite		
	JLSB18	1.70	Pyrite		
	JLSB19	2.10	Pyrite		
Baqata	JLSB12	6.00	Pyrite		
	JLSB25	5.50	Pyrite		
	JLSB27	8.90	Pyrite		
	JLSB26	11.80	Pyrite		
	JLSB21	-4.60	Pyrite		
Kabe West	JLSB23	-3.50	Pyrite		
	KBP01	-4.08	Pyrite		
	KBP02	1.06	Pyrite		
	KBP03	1.36	Pyrite		
	KBP05	-0.65	Pyrite		
	KBP11	1.95	Pyrite		
	KBP12	1.82	Pyrite		
	JLSB22	3.40	Pyrite		
	<b>Skarns</b>				
	Karakaene Ndi	JLSB01	4.40	Pyrite	Disseminated
JLSB03		4.20	Pyrite	Disseminated	
JLSB04		3.80	Pyrite	Disseminated	
JLSB05		4.10	Pyrite	Disseminated	
JLSB34 (2)		3.10	Pyrite	Disseminated	
JLSB35		2.80	Pyrite	Disseminated	
JLSB33		4.00	Pyrite	Fe-oxide vein	
JLSB36		7.00	Pyrite	Sulphide vein	
JLSB37		8.07	Pyrite	Sulphide vein	
JLSB38		11.90	Pyrite	Sulphide vein	
JLSB39	4.90	Pyrite	Sulphide vein		
<b>Loulo Au deposits</b>					
Faraba	‡FA20	10.60	Pyrite		
	‡FA04	11.40	Pyrite		
	‡FA10	11.90	Pyrite		
	‡FA23	12.60	Pyrite		
	†PT5	15.20	pyrite		
	†PT6	15.50	pyrite		
	†LD13	14.10	pyrite		

	†LD20	13.60	pyrite
	†LD30	13.80	pyrite
	†LD38	14.50	pyrite
	†LD44	11.70	pyrite
	†LD45	13.30	pyrite
Gara	†LD46	11.50	pyrite
	†LD51	14.30	pyrite
	†LD53	12.50	pyrite
	*C13-100.55	12.10	pyrite
	*C23-26.0	12.90	pyrite
	*C23-198.3b	12.50	pyrite
	*C23-198.55	12.90	pyrite
	*C2-17.75	12.90	pyrite
	†LD54	7.00	Pyrite
	‡JLS01	8.20	Pyrite
	‡JLS02	7.00	Pyrite
	‡JLS03	8.40	Pyrite
	‡JLS05	9.50	Pyrite
	‡LS06	10.00	Pyrite
	‡JLS10 (2)	7.10	Pyrite
	‡JLS12	12.50	Pyrite
Goukoto	‡JLS19	7.00	Pyrite
	‡JLS20	9.70	Pyrite
	‡JLS21	12.80	Pyrite
	‡JLS22	5.90	Pyrite
	‡JLS23	8.00	Pyrite
	‡JLS27	9.60	Pyrite
	‡JLS31	10.30	Pyrite
	‡JLS33	9.70	Pyrite
	‡JLS34	6.25	Pyrite
	*C4-18.20	9.20	pyrite
	*C4-21.00	7.80	pyrite
Loulo-3	*C4-16.00	8.90	pyrite
	*C4-18.20	9.20	pyrite
	*C4-21.00	7.80	pyrite
	*C4-16.00	8.90	pyrite
P125	†PT13	6.70	Pyrite
	*C3-51.9	8.90	pyrite
	*C1-46.0a	9.20	pyrite
	*C1-46.0b	8.70	pyrite
	*C1-46.0c	8.10	pyrite
	*C12-72.4	6.00	pyrite
	*C2-54.9	6.70	pyrite
	*C1-44.0	6.90	pyrite
	*C1-41.5	7.70	pyrite
	*C1-43.9	7.30	pyrite
	*C3-35.6	7.80	pyrite
P-64	*C14-60.85	6.70	pyrite
	*C12-45.3	8.40	pyrite
	*C14.58.8	8.00	pyrite

	*C4-31.75	9.50	pyrite
	*C4-41.95	10.50	pyrite
	*C4-34.5	8.70	pyrite
	*C10-58.0	8.80	pyrite
	*C4-64.5	8.60	pyrite
	*C4-38.2	9.10	pyrite
	*C13-68.0	9.50	pyrite
	*C6-120.7	9.70	pyrite
	*C14-58.8	7.00	pyrite
	†PT18	7.30	pyrite
	†PT20	8.00	pyrite
	†PT26	8.80	pyrite
Yalea	†07YD60	8.30	pyrite
	†07YD65	7.10	pyrite
	†07YD76	7.70	pyrite
	†YD11	9.20	Pyrite

Deposit/target Name	Sample	$\delta^{13}\text{CPDB}$ (‰)	$\delta^{18}\text{OSMOW}$ (‰)	Grade (ppm)	Sample type
<b>Host Rock</b>					
Host Dolostone (Baqata)	JLSB9	-1.44	19.10	<0.01	Host rock
Host Dolostone (Gara)	†G13	1.30	23.20	<0.01	Host rock
	†LD16	-0.40	20.70	<0.01	Host rock
	†LD26	0.10	23.30	<0.01	Host rock
	*C23-26	0.50	22.20	<0.01	Host rock
Host Dolostone (Goukoto)	‡JLS11	-0.25	19.75	<0.01	Host rock
	‡JLS32	-3.13	19.26	<0.01	Host rock
Host Dolostone (Kolya)	JLSB7	1.11	15.07	<0.01	Host rock
Host Dolostone (Yalea)	†07YD52	-2.90	20.00	<0.01	Host rock
	†07YD53	0.40	19.90	<0.01	Host rock
<b>Barren veins</b>					
Baqata	JLSB10	-1.74	15.31	<0.01	Vein
Gara	†G39	-0.20	17.40	<0.01	Vein
	†G40	-1.70	21.10	<0.01	Vein
	*C13-114.7	-2.00	15.10	<0.01	Vein
	*C23-84	3.80	16.90	<0.01	Vein
Goukoto	‡JLS18	-2.35	18.23	<0.01	Vein
	‡JLS29	-0.49	18.18	<0.01	Vein
Kolya	JLSB24	0.22	15.21	<0.01	Vein
Yalea	†07YD90	-1.70	16.40	<0.01	Vein
<b>Loulo Au deposits</b>					
Gara	†PT5	-10.50	15.20	3.36	Vein
Gara	†PT9	-11.90	15.40	86.40	Vein
Gara	†LD13	-13.70	15.40	31.40	Vein
Gara	†LD20	-11.60	15.60	90.30	Vein
Gara	†LD31	-13.10	15.50	6.20	Vein
Gara	†LD32	-9.70	15.50	27.80	Vein
Gara	†LD44	-14.40	15.60	8.20	Vein
Gara	†LD45	-11.60	15.10	4.65	Vein
Gara	†LD46	-8.60	15.20	26.80	Vein
Gara	*C13-100.55	-5.90	16.00	-	Vein
Gara	*C23-198.3a	-6.50	17.70	-	Vein
Gara	*C23-198.3b	-4.50	19.50	-	Vein
Gara	*C14-112.5	-5.10	15.50	-	Vein
Gara	*C6-41	-7.20	15.70	-	Vein
Goukoto	‡JLS06	-11.15	19.15	35.10	Vein
Goukoto	‡JLS12	-13.60	16.25	7.80	Vein
Goukoto	‡JLS25	-6.30	17.71	-	Vein
Goukoto	‡JLS26	-9.44	20.47	-	Vein
Goukoto	‡JLS28	-6.68	15.16	<0.01	Vein
Goukoto	‡JLS33	-8.93	14.92	2.90	Vein
Goukoto	‡JLS34	-9.03	19.77	0.26	Vein
Goukoto	‡JLS35	-7.99	14.73	0.04	Vein
Yalea Main	†07YD69	-15.80	23.20	15.98	Vein
Yalea Main	†08YD10	-19.50	15.10	-	Vein
Yalea Main	†07YD71	-21.50	14.40	9.43	Wall rock alteration
Yalea Main	†07YD76	-21.70	14.20	5.51	Wall rock alteration
Yalea Main	†08YD24	-15.90	13.50	5.51	Wall rock alteration
Yalea Main	†08YD33	-16.10	14.80	7.80	Wall rock alteration
Faraba	FA20	-6.63	15.42	4.57	Vein
Faraba	FA6	-13.20	20.50	0.34	Vein
Faraba	FA7	-12.20	18.20	0.45	Vein
Faraba	FA12	-10.90	18.50	4.98	Vein

P-64	*C2-52	-7.00	16.90	-	Vein
P-64	*C4-75.5	-8.50	19.10	-	Vein
<b>Target</b>					
Baqata	JLSB11	-3.74	15.42	<0.01	Vein
Baqata	JLSB26	-14.97	14.47	0.13	Vein
Baqata	JLSB28	-8.58	14.46	<0.01	Vein
Baqata	JLSBP10	-6.46	13.35	<0.01	Vein
Baqata	JLSBP12	-5.53	13.03	<0.01	Vein
Baqata	JLSBP17	-12.28	16.48	<0.01	Vein
Boboti	JLSB17	-5.27	11.88	0.04	Vein
Boboti	JLSB18	-5.68	12.15	<0.01	Vein
Gefa	JLSBP44	-16.80	13.41	0.01	Vein
Gefa	JLSBP46	-7.92	17.18	0.01	Vein
Gefa	JLSBP51	-7.02	11.39	0.01	Vein
Gefa	JLSBP55	-9.03	13.86	0.01	Vein
Kabe West	JLSB21	-7.27	13.32	11.53	Vein
Kabe West	JLSB22	-8.47	13.34	0.56	Vein
Kabe West	KBP01	-6.55	14.77	11.33	Vein
Kabe West	KBP03	-5.88	13.82	2.05	Vein
Kabe West	KBP06	-8.58	13.85	0.20	Vein
Kabe West	KBP12	-6.66	13.25	0.01	Vein
Kolya	JLSB29	-7.47	14.85	0.39	Vein
Kolya	JLSB30	-8.84	14.35	0.16	Vein
Kolya	JLSB31	-8.52	14.58	0.08	Vein
Kolya	JLSB32	-8.60	14.69	0.60	Vein

	wt. % NaCl equiv.	X <sub>H2O</sub>	X <sub>NaCl</sub>	X <sub>CO2</sub>	m <sub>H2O</sub>	m <sub>NaCl</sub>	m <sub>CO2</sub>	δ <sup>13</sup> C <sub>i</sub> (‰)	δ <sup>18</sup> O <sub>i</sub> (‰)
Kofi Series evaporite brine	41.70	0.70	0.25	0.05	38.86	4.28	1.14	1.80	17.25
Metamorphic fluid	6.10	0.78	0.02	0.20	43.19	0.38	4.54	-27.00	10.20
Magmatic Fluid	3.30	0.82	0.02	0.16	45.67	0.30	3.64	-6.00	9.40

3.5E+08